
DATA COMPLETION FOR ELECTRICAL IMPEDANCE TOMOGRAPHY BY CONDITIONAL DIFFUSION MODELS

Ke Chen

Department of Mathematical Sciences
University of Delaware
kechen@udel.edu

Haizhao Yang

Department of Mathematics
Department of Computer Science
University of Maryland, College Park
hzyang@umd.edu

Chugang Yi*

Department of Mathematics
University of Maryland, College Park
chugang@umd.edu

ABSTRACT

Data scarcity is a fundamental barrier in Electrical Impedance Tomography (EIT), as undersampled Dirichlet-to-Neumann (DtN) measurements can substantially degrade conductivity reconstructions. We address this bottleneck by completing partially observed DtN measurements using a diffusion-based generative model. Specifically, we train a conditional diffusion model to learn the distribution of DtN data and to infer full measurement vectors given partial observations. Our approach supports flexible source-receiver configurations and can be used as a plug-in preprocessing step with off-the-shelf EIT solvers. Under mild assumptions on the polygon conductivity class, we derive nonasymptotic end-to-end bounds on the distributional discrepancy between the completed and ground-truth DtN measurements. In numerical experiments, we couple the proposed diffusion completion procedure with a deep learning-based inverse solver and compare its performance against the same solver with full measurement data. The results show that diffusion completion enables reconstructions that closely match the full-data baseline while using only 1% of the measurements. In contrast, standard baselines such as matrix completion require 30% of the measurements to achieve similar reconstruction quality.

1 Introduction

Inverse problems governed by partial differential equations (PDEs) arise across a broad range of scientific and engineering domains, including medical imaging [Arridge, 1999, Cheney et al., 1990, Borcea, 2002], geophysical exploration [Tarantola and Valette, 1982, Pratt, 1999], and materials characterization [Bonnet and Constantinescu, 2005, García-Martín et al., 2011]. Many such inverse problems are nonlinear and severely ill-posed [Bal, 2012, Uhlmann, 2009, Isakov, 2006], and Electrical Impedance Tomography (EIT) is a canonical example of these difficulties [Alessandrini, 1988, Allers and Santosa, 1991]. In EIT, the goal is to determine the conductivity distribution within a medium by applying voltage patterns on its boundary and measuring the induced current responses. One of the key components of EIT is the Dirichlet-to-Neumann (DtN) operator, which maps voltage patterns to current responses. Theoretically, the conductivity can be uniquely determined from full knowledge of the DtN operator under mild conditions [Nachman, 1996, Astala and Päivärinta, 2006, Uhlmann, 2013, Sylvester and Uhlmann, 1987]. In practice, the continuous DtN operator is often discretized into a *DtN matrix* containing voltage-current measurements on a finite number of boundary nodes. Typical methods for solving EIT include iterative solvers with regularization [Hanke, 1997, Haber et al., 2000, Jin et al., 2012, Vauhkonen et al., 2002], direct methods [Chow et al., 2021, 2014, Mueller and Siltanen, 2020], and recent deep learning approaches [Hamilton and Hauptmann, 2018, Ong et al., 2022, Guo et al., 2023, Cen et al., 2023, Chen et al., 2024, Molinaro et al., 2023, Bhat et al., 2025]. However, when only limited measurements are available, as

*Corresponding author. Authors are listed in alphabetical order.

is common in medical imaging [Heines et al., 2023, Putensen et al., 2019, Scaramuzzo et al., 2024], reconstruction pipelines that presuppose fully sampled DtN measurements often fail to produce reliable solutions. The scarcity or incompleteness of measurements thus poses a central challenge in practical EIT.

To address a limited measurement budget, active acquisition strategies such as optimal experimental design (OED) and reinforcement learning (RL) aim to identify measurement configurations or sensing policies that extract the most informative measurements from a limited number of experiments. Their effectiveness has been demonstrated in EIT [Hyvönen et al., 2024, Jin et al., 2024] and other inverse problems [Huan and Marzouk, 2013, Shen et al., 2022, Alexanderian, 2021, Jiang et al., 2024, Go and Chen, 2025, Koval and Nicholson, 2025]. Although these approaches can improve the quality of the collected data, they typically require many forward and inverse solves. Moreover, partial measurements can hinder the use of off-the-shelf reconstruction methods that expect complete measurements. For instance, in inverse scattering, limited aperture data leads to artifacts known as “shadow regions” [Colton and Monk, 2006, Li et al., 2015], while in EIT partial boundary data exacerbates the loss of spatial resolution and causes geometrical distortion [Hauptmann, 2017, Alsaker et al., 2017].

Another line of work seeks to reconstruct the full measurements from partial observations in many inverse problems [Harrach, 2015, Hauptmann, 2017, Caubet et al., 2019, Dou et al., 2022, Bui-Thanh et al., 2022], thereby bridging the gap to inverse solvers that presuppose complete measurements. For EIT, Harrach [2015] predict the missing voltages on current-driven boundary nodes in the difference Neumann-to-Dirichlet (DtD) matrix, relying on the geometry-dependent smoothness of difference DtD data; Hauptmann [2017] approximate continuum DtD data from boundary measurements via a two-stage optimization that first lifts voltages to smooth boundary traces using Tikhonov regularization and then applies a prior-regularized least-squares fit to recover an approximate full DtD map; and the most closely related work, Bui-Thanh et al. [2022], completes unobserved entries in the off-diagonal blocks of the hierarchically partitioned DtD matrix by exploiting the low-rank structure inherited from the underlying elliptic operator [Bebendorf and Hackbusch, 2003]. Specifically, Bui-Thanh et al. [2022] achieve high-accuracy completion when the off-diagonal blocks of the DtD matrix are randomly sampled at a moderate sampling rate.

These EIT data completion methods [Harrach, 2015, Hauptmann, 2017, Bui-Thanh et al., 2022] leverage PDE-induced smoothness or low-rank structure, but may become less reliable under highly structured missingness, extremely sparse electrode layouts, or strong measurement noise. They typically perform completion in an instance-wise manner, requiring a problem-specific interpolation, regularization or matrix-completion routine to be executed for each new measurement set and acquisition configuration. In contrast, we propose a data-driven completion framework based on conditional diffusion models. By exploiting the low-dimensional structure of the conductivity distribution, our method amortizes completion across instances and enables accurate DtD completion under flexible and challenging measurement configurations. Diffusion models, also known as score-based generative models, have achieved remarkable success in learning complex distributions from high-dimensional data [Song et al., 2020b, Ho et al., 2020], and recent theory shows that they effectively capture low-dimensional structure in high-dimensional distributions [Tang et al., 2024, Azangulov et al., 2024, Liang et al., 2025], a property that has been leveraged in recent EIT works [Alberti et al., 2022, 2024]. Building on the low-dimensional manifold structure of the conductivity distribution and the continuity of the forward map with respect to the conductivity, we show that the induced distribution of DtD measurements can be learned efficiently using a conditional diffusion model. The main contributions of this work can be summarized as follows:

- **DtD completion via conditional diffusion.** To the best of our knowledge, this is the first framework that learns the distribution of (discrete) DtD measurements via a diffusion model and performs DtD completion by posterior sampling conditioned on partial observations.
- **Extreme undersampling performance.** Due to the ill-posedness of EIT, DtD measurements from different conductivities can be nearly indistinguishable, which hinders learning under heavy missingness. Our EIT-tailored normalization enhances contrast across measurements and stabilizes optimization of the neural network, enabling accurate completion from only 1% of the measurements, a regime in which low-rank matrix completion fails.
- **Flexible measurement configurations.** Whereas matrix completion relies on random missingness, our method accommodates flexible source–receiver patterns by encoding partial measurements as conditioning inputs to the score network. Thus our model can learn to infer missing entries under varied masks, providing robust completion under diverse measurement configurations.
- **Convergence guarantees.** By bridging diffusion models and EIT theory, we establish non-asymptotic end-to-end bounds for our DtD completion algorithm for polygonal conductivities.
- **Plug-and-play with inverse solvers.** The completed measurements can be used as a preprocessing step for off-the-shelf EIT solvers; when preceded by our completion step, a deep inverse network yields substantially better reconstructions than the same architecture trained directly on partial data.

The remainder of the paper is organized as follows. Section 2 formalizes the problem; Section 3 presents our diffusion completion framework for DtN measurements; Section 4 develops the error analysis; and Section 5 reports numerical results.

2 Problem Setup

Let $\Omega \subset \mathbb{R}^2$ be the unit disk, i.e., $\Omega = \{(x, y) \mid x^2 + y^2 < 1\} \subset \mathbb{R}^2$. The unknown parameter of interest is the conductivity $\gamma : \Omega \rightarrow \mathbb{R}^+$, where $\gamma(x)$ represents the conductivity at point $x \in \Omega$ and \mathbb{R}^+ denotes the set of positive real numbers. The forward problem is to solve the elliptic equation

$$\nabla \cdot (\gamma(x) \nabla u(x)) = 0 \quad \text{in } \Omega, \quad u(x) = f(x) \quad \text{on the boundary } \partial\Omega, \quad (1)$$

where $f : \partial\Omega \rightarrow \mathbb{R}$ is a prescribed voltage function on the boundary $\partial\Omega$. The resulting solution $u_\gamma^f(x)$ of Equation 1 determines the induced boundary current

$$g(x) = \gamma(x) \frac{\partial u_\gamma^f}{\partial n}(x) \quad \text{on } \partial\Omega, \quad (2)$$

where $\frac{\partial}{\partial n}$ denotes the outward normal derivative. The mapping $f \mapsto g$ in Equation 2 defines the Dirichlet-to-Neumann operator

$$\Lambda_\gamma : H^{1/2}(\partial\Omega) \rightarrow H^{-1/2}(\partial\Omega), \quad (3)$$

which takes a boundary voltage function f on $\partial\Omega$ and returns the corresponding boundary current g . Here $H^{\pm 1/2}(\partial\Omega)$ is the standard Sobolev Hilbert spaces on $\partial\Omega$ with inner products $\langle \cdot, \cdot \rangle_{H^{\pm 1/2}}$ and norms $\|\cdot\|_{H^{\pm 1/2}}$.

The weak form of Equation 1 can be formulated as find $u \in H^1(\Omega)$, $u|_{\partial\Omega} = f$ such that

$$\int_{\Omega} \gamma(x) \nabla u \cdot \nabla v \, dx = 0, \quad \forall v \in H_0^1(\Omega). \quad (4)$$

Thus we could define DtN operator

$$\langle \Lambda_\gamma f, \psi \rangle = \int_{\partial\Omega} \gamma \frac{\partial u_\gamma^f}{\partial n} \psi \, ds. \quad (5)$$

for $\psi \in H_0^{1/2}(\partial\Omega)$.

In EIT, we aim to recover $\gamma(x)$ from multiple data pairs $\{(f_i, g_i)\}$, where the input boundary voltage f_i depends on experimental design. Ideally, if one could measure g for all admissible f , $\gamma(x)$ can be recovered in theory [Uhlmann, 2009, Isakov, 2006, Astala and Päivärinta, 2006]. However, as infinitely many measurements are not attainable, using a finite number of measurement pairs (f_i, g_i) is of more interest in practice.

Finite element discretizations We approximate Ω by a polygonal domain Ω_h with a shape-regular triangulation \mathcal{T}_h and use the linear (P_1) finite element space $V_h \subset H^1(\Omega_h)$ of continuous, piecewise-linear functions on \mathcal{T}_h . Let $\{\phi_k\}_{k=1}^{N_{\text{el}}}$ be the nodal basis of V_h , and split the indices into interior nodes \mathcal{I} with $N_{\mathcal{I}} = |\mathcal{I}|$ and boundary nodes \mathcal{B} with $N_{\mathcal{B}} = |\mathcal{B}|$. Define the subspace $V_h^0 = \{v^h \in V_h : v^h|_{\partial\Omega_h} = 0\}$ and the trace space $V_h(\partial\Omega_h) = \text{span}\{\phi_j|_{\partial\Omega_h}, j \in \mathcal{B}\}$. Given boundary data $f^h \in V_h(\partial\Omega_h)$, Equation 4 now can be discretized as follows:

$$\text{Find } u^h \in V_h \text{ with } u^h|_{\partial\Omega_h} = f^h, \text{ such that } a(u^h, v^h) = \int_{\Omega_h} \gamma \nabla u^h \cdot \nabla v^h \, dx = 0, \quad \forall v^h \in V_h^0.$$

We assemble the stiffness matrix $\mathbf{K} \in \mathbb{R}^{N_{\text{el}} \times N_{\text{el}}}$ with entries $\mathbf{K}_{ij} = a(\phi_i, \phi_j)$ and denote by \mathbf{u} , \mathbf{f} and \mathbf{g} the corresponding vectors by tabulating its coefficient of the FEM basis $\{\phi_i\}_{i \in \mathcal{B} \cup \mathcal{I}}$ for u^h , f^h and g^h respectively.

We partition \mathbf{K} and \mathbf{u} with index sets \mathcal{I} and \mathcal{B} with

$$\mathbf{K} = \begin{bmatrix} \mathbf{K}_{\mathcal{I}\mathcal{I}} & \mathbf{K}_{\mathcal{I}\mathcal{B}} \\ \mathbf{K}_{\mathcal{B}\mathcal{I}} & \mathbf{K}_{\mathcal{B}\mathcal{B}} \end{bmatrix} \quad \text{and} \quad \mathbf{u} = \begin{bmatrix} \mathbf{u}_{\mathcal{I}} \\ \mathbf{u}_{\mathcal{B}} \end{bmatrix}.$$

Let the discrete Neumann data vector $\mathbf{g} \in \mathbb{R}^{N_{\mathcal{B}}}$ be defined by $g_j = a(u^h, \phi_j)$ for $j = 1, \dots, N_{\mathcal{B}}$. Eliminating the interior degrees of freedom yields the block relation

$$\mathbf{g} = \mathbf{K}_{\mathcal{B}\mathcal{B}}\mathbf{f} + \mathbf{K}_{\mathcal{B}\mathcal{I}}\mathbf{u}_{\mathcal{I}} = \underbrace{(\mathbf{K}_{\mathcal{B}\mathcal{B}} - \mathbf{K}_{\mathcal{B}\mathcal{I}}\mathbf{K}_{\mathcal{I}\mathcal{I}}^{-1}\mathbf{K}_{\mathcal{I}\mathcal{B}})}_{\Lambda_\gamma}\mathbf{f}. \quad (6)$$

Therefore, the discrete DtN matrix Λ_γ is the Schur complement of the stiffness matrix \mathbf{K} with respect to the interior block $\mathbf{K}_{\mathcal{I}\mathcal{I}}$. If the k -th experiment impose the canonical boundary voltage $\mathbf{f} = \mathbf{e}_k$, then $\mathbf{g} = \Lambda_\gamma \mathbf{e}_k$, so the corresponding Neumann measurement vector is exactly the k -th column of Λ_γ . Consequently, under the canonical set of boundary excitations, Λ_γ coincides with the complete discrete current-measurement table on the prescribed boundary node set. More generally, for a multi-source experiment, we collect all boundary voltage vectors $\{\mathbf{f}_k\}$ as the columns of a matrix $\mathbf{F} \in \mathbb{R}^{N_B \times N_B}$, and the associated Neumann measurements are then assembled as $\Lambda_\gamma \mathbf{F}$. Without loss of generality, we restrict attention to the canonical experiment design $\mathbf{F} = \mathbf{I}$, in which case the measurement matrix coincides with the DtN matrix.

Partial observations and data completion Ideally, if all chosen boundary nodes are applied and the currents are measured at all boundary nodes, one would fully determine the $N_B \times N_B$ DtN matrix Λ_γ . However, practical and economic constraints often prevent running all possible experiments or taking all desired measurements. In practice, only a small number of experiments can be conducted, and in each experiment, only a small number of measurements can be taken, which results in only a subset of DtN matrix entries being measured. Let $\mathbf{M}_s \in \{0, 1\}^{N_B \times N_B}$ be a binary mask matrix with $(\mathbf{M}_s)_{ij} = 1$ if the entry (i, j) is observed and 0 otherwise, where $s = \frac{\|\mathbf{M}_s\|_0}{N_B^2}$ is the sampling rate, i.e., the portion of observed entries over all entries. Thus the *configuration* of how we obtain the DtN measurements is encoded by \mathbf{M}_s , and the observed (incomplete) DtN measurements are denoted by

$$\Lambda_\gamma^o = \mathbf{M}_s \odot \Lambda_\gamma,$$

where \odot denotes the Hadamard product. We emphasize that \mathbf{M}_s is an abstract encoding of the acquisition pattern and may represent highly structured missingness (e.g., missing columns corresponding to unperformed excitations, or subsampled receiver sets), not necessarily i.i.d. entrywise sampling.

Given the masked DtN matrix Λ_γ^o and mask \mathbf{M}_s , our completion task is to infer the missing entries, i.e. estimate a completed matrix $\hat{\Lambda}_\gamma$ that is close to the true Λ_γ .

3 Method

In this section, we will formulate the data completion problem by conditional sampling solved by diffusion model. As multiple completions may plausibly explain the same partial observations, we model Λ_γ as a random matrix whose randomness comes from some distribution of γ and the goal is to generate samples from the learned conditional distribution $p(\Lambda_\gamma \mid \Lambda_\gamma^o, \mathbf{M}_s)$. The generated posterior samples can then be used to estimate the full DtN matrix $\hat{\Lambda}_\gamma$, and standard inverse solvers including iterative solvers, optimization-based reconstruction, or deep learning-based methods can be applied to recover conductivity γ . The key is to ensure that $\hat{\Lambda}_\gamma$ is as close as possible to the true underlying operator Λ_γ , thereby achieving better results in the downstream inversion than the same solver without completion.

3.1 Diffusion Model

Given i.i.d. samples from a target distribution p_{target} , a diffusion model seeks to generate new samples whose distribution approximates p_{target} . Let $\{\alpha_t\}_{t=1}^T \subset (0, 1]$ and define $\bar{\alpha}_t := \prod_{i=1}^t \alpha_i$. Define the forward Markov chain by $X_0 \sim p_{\text{target}}$ and, for $t = 1, \dots, T$, $X_t = \sqrt{\alpha_t} X_{t-1} + \sqrt{1 - \alpha_t} W_t$ with $W_t \stackrel{\text{i.i.d.}}{\sim} \mathcal{N}(0, I_d)$; equivalently, $X_t \mid X_0 \sim \mathcal{N}(\sqrt{\bar{\alpha}_t} X_0, (1 - \bar{\alpha}_t) I_d)$, hence $X_t = \sqrt{\bar{\alpha}_t} X_0 + \sqrt{1 - \bar{\alpha}_t} \bar{W}$ for $\bar{W} \sim \mathcal{N}(0, I_d)$. This construction progressively perturbs X_0 with Gaussian noise over $t = 1, \dots, T$. The noise schedule $\{\alpha_t\}$ is chosen so that $\bar{\alpha}_T \approx 0$, in which case the marginal distribution of X_T is close to a standard Gaussian, i.e., $p_{X_T} \approx \mathcal{N}(0, I_d)$.

The forward process is reversible as shown in classical results from stochastic differential equation (SDE) [Anderson, 1982], which inspires the sampling algorithm from diffusion model. The key aspect of the sampling algorithm from diffusion model is to construct a reverse process Y_t , which starts from pure Gaussian noise and can gradually convert to a new sample Y_0 such that $p_{Y_0} \approx p_{\text{target}}$. In particular, the reverse process relies on the availability of the so called *score function* $s_t^*(\cdot) := \nabla \log p_{X_t}(\cdot)$, thus diffusion model is also called score-based generative model Song et al. [2020b]. A classical choice of reverse process is the Denoising Diffusion Probabilistic Model (DDPM) [Ho et al., 2020] sampler as follows, which can be treated as a discretization of reverse SDE.

Definition 3.1 (Unconditional DDPM sampler). *Given score estimator $s_t(\cdot)$ that approximate the true score function $s_t^*(\cdot)$, i.e., $s_t(\cdot) \approx s_t^*(\cdot)$ and the same noise schedule $\{\alpha_t\}$ as in forward process, DDPM sampler is defined as*

$$Y_T \sim \mathcal{N}(0, I_d), \quad Y_{t-1} = \frac{1}{\sqrt{\alpha_t}} \left(Y_t + (1 - \alpha_t) s_t(Y_t) + \sigma_t W_t \right), \quad W_t \stackrel{\text{i.i.d.}}{\sim} \mathcal{N}(0, I_d), \quad (7)$$

with

$$\sigma_t = \sqrt{\frac{(\alpha_t - \bar{\alpha}_t)(1 - \alpha_t)}{1 - \bar{\alpha}_t}}, \quad t = T, \dots, 1. \quad (8)$$

When a score estimator $s_t(\cdot) \approx s_t^*(\cdot)$ is available, DDPM sampler 3.1 provides a way to generate new samples from the target distribution [Ho et al., 2020]. In practice, the score estimator is parametrized by a neural network $s_\theta(\cdot, t)$, and the parameters θ can be learned through the *score matching loss* [Ho et al., 2020, Song et al., 2020b, Vincent, 2011]:

$$\min_{\theta} \mathbb{E}_{t \sim \text{Unif}(1, \dots, T), X_0 \sim p_{\text{target}}, X_t \sim p_{X_t | X_0}} \lambda(t) \|s_\theta(X_t, t) - \nabla_{x_t} \log p(X_t | X_0)\|^2, \quad (9)$$

where t follows a uniform distribution over $1, 2, \dots, T$, $\lambda(t)$ is a positive weighting function, and $\nabla \log p(X_t | X_0)$ can be computed *analytically* from the forward diffusion process. Concretely, the expectation can be approximated by the Monte Carlo estimation. Each training iteration (1) draws a batch $\{X_0^{(i)}\}_{i=1}^B$ with size B from dataset $\mathcal{D}_{\text{train}}$, (2) samples an independent time step $t_i \sim \mathcal{D}\mathcal{U}\{1, \dots, T\}$ and noise $W^i \sim \mathcal{N}(0, I_d)$ for each sample, and (3) forms a noised input

$$X_{t_i}^{(i)} = \sqrt{\bar{\alpha}_{t_i}} X_0^{(i)} + \sqrt{1 - \bar{\alpha}_{t_i}} W^i. \quad \text{We then compute the regression target } s_{t_i}(X_{t_i}^{(i)}) = -\frac{X_{t_i}^{(i)} - \sqrt{\bar{\alpha}_{t_i}} X_0^{(i)}}{1 - \bar{\alpha}_{t_i}}, \quad \text{evaluate}$$

the weighted mean-squared error $\lambda(t_i) \|s_\theta(X_{t_i}^{(i)}, t_i) - s_{t_i}(X_{t_i}^{(i)})\|^2$ over the batch, and update θ with standard deep learning solver, e.g. AdamW [Loshchilov and Hutter, 2017]. At the population level, Equation 9 is minimized when $s_\theta(\cdot, t)$ matches the true marginal score $s_t^*(x) := \nabla_x \log p_t(x)$ (where p_t is the law of X_t induced by the forward diffusion); in well-specified and identifiable parametric settings, minimizers of the empirical (Monte Carlo) counterpart converge in probability to a population minimizer and hence yield a consistent score estimator [Hyvärinen and Dayan, 2005, Song et al., 2020b].

With standard assumptions on sufficiency of the model capacity, the optimal solution of Equation 9, denoted as θ^* , is a consistent estimator, i.e., it converges in probability towards the true value of θ when sample size goes infinity [Song et al., 2020b, Hyvärinen and Dayan, 2005].

3.2 Conditional Diffusion Models for Data Completion

Diffusion model is also flexible in incorporating a conditional covariate, denoted as Z , to guide the generation of new samples. For each fixed $Z = z$, DDPM sampler 3.1 can be extended to conditional generation when the conditional score estimator $s_t(\cdot, z) \approx s_t^*(\cdot, z)$ is given, where $s_t^*(\cdot, z) = \nabla \log p_{X_t | Z}(\cdot)$. The following conditional DDPM sampler can generate a new sample Y_0 such that $p_{Y_0} \approx p_{X_0 | Z=z}$.

Definition 3.2 (Conditional DDPM sampler). *For a fixed $Z = z$, given conditional score estimator $s_t(\cdot, z)$ that approximate the true conditional score function $s_t^*(\cdot, z)$, i.e. $s_t(\cdot, z) \approx s_t^*(\cdot, z)$, the conditional DDPM sampler is defined as*

$$Y_T \sim \mathcal{N}(0, I_d), \quad Y_{t-1} = \frac{1}{\sqrt{\alpha_t}} \left(Y_t + (1 - \alpha_t) s_t(Y_t, z) + \sigma_t W_t \right), \quad W_t \stackrel{i.i.d.}{\sim} \mathcal{N}(0, I_d). \quad (10)$$

Here $\alpha_t, \bar{\alpha}_t, \sigma_t$ are the same as defined in unconditional DDPM sampler 3.1.

The conditional score function can also be parametrized by a neural network $s_\theta(\cdot, z, t)$, and learned by following conditional score matching,

$$\min_{\theta} \mathbb{E}_{t \sim \text{Unif}(1, \dots, T), (X_0, Z) \sim p_{(X_0, Z)}, X_t \sim p_{X_t | X_0}} \lambda(t) \|s_\theta(X_t, Z, t) - \nabla_{x_t} \log p(X_t | X_0)\|^2, \quad (11)$$

where $p_{(X_0, Z)}$ is the joint distribution of target X_0 and condition Z . Although $p_{X_t | Z}$ does not appear in the loss function explicitly, it has been proved in Batzolos et al. [2021], Vincent [2011] that $s_{\theta^*}(X, Z, t)$ is a consistent estimator of $\nabla \log p(X_t | Z)$ under some standard assumptions, where θ^* is the minimizer of Equation 11. In practice we approximate the expectation in Equation 11 with the same Monte Carlo scheme as in the unconditional case, except that each training example carries its condition Z and the network receives (X_t, Z, t) as input.

Recall that in EIT data completion, our goal is to sample $p(\Lambda_\gamma | \Lambda_\gamma^0, \mathbf{M})$ for any given partial DtN measurements Λ_γ^0 and mask \mathbf{M} . We instantiate the conditional diffusion model by setting target variable $X_0 = \Lambda_\gamma$ and conditional variable $Z = (\Lambda_\gamma^0, \mathbf{M})$. Throughout, we identify a DtN matrix $X_0 \in \mathbb{R}^{N_B \times N_B}$ with its vectorization $\text{vec}(X_0) \in \mathbb{R}^d$, $d = N_B^2$; the forward/noising and reverse/sampling updates are applied to $\text{vec}(X_0)$, and the matrix form is only a reshape used for notation and implementation. Concretely, suppose various configurations \mathbf{M} follow some distribution \mathcal{M} , we draw full DtN measurements $\{\Lambda_{\gamma_i}\}_{i=1}^B$ from $\mathcal{D}_{\text{train}}$ and $\{\mathbf{M}^{(i)}\}_{i=1}^B \sim \mathcal{M}$. For each i , we form the pair sample

$$\{X_0^{(i)}, Z^i\} = \{\Lambda_{\gamma_i}, (\mathbf{M}^{(i)} \odot \Lambda_{\gamma_i}, \mathbf{M}^{(i)})\},$$

which yields samples from the joint distribution $p(X_0, Z)$. The conditional score $s_\theta(X_t, Z, t)$ is then trained exactly as in Equation 11. At test time, for a given partially observed DtN measurements $\Lambda_\gamma^o = \mathbf{M}^{\text{test}} \odot \Lambda_\gamma^{\text{test}}$, we set $Z_{\text{test}} = (\Lambda_\gamma^o, \mathbf{M}^{\text{test}})$ and run the conditional DDPM sampler 3.2 to generate $\widehat{\Lambda}_\gamma = Y_0$ such that $\widehat{\Lambda}_\gamma \approx \Lambda_\gamma^{\text{test}}$. The training and sampling pseudo-codes are summarized in Algorithm 1 and Algorithm 2, respectively.

Algorithm 1 Training the conditional score network for DtN measurements completion

Require: Fully observed DtN dataset $\mathcal{D}_{\text{train}} = \{\Lambda_{\gamma_i}\}_{i=1}^{N_{\text{train}}}$; measurement configuration distribution \mathcal{M} ; schedule $\{\alpha_t\}_{t=1}^T$, weight $\lambda(t)$, batch size B ; conditional score network $s_\theta(X_t, Z, t)$ to be optimized and optimizer

- 1: **while** not converged **do**
- 2: Sample $\{\Lambda_{\gamma_i}\}_{i=1}^B$ from $\mathcal{D}_{\text{train}}$, and $\{\mathbf{M}^{(i)}\}_{i=1}^B \sim \mathcal{M}$
- 3: Set $X_0^{(i)} \leftarrow \Lambda_{\gamma_i}$ and conditions $Z^i \leftarrow (\mathbf{M}^{(i)} \odot \Lambda_{\gamma_i}, \mathbf{M}^{(i)})$
- 4: Sample batch $\{t_i\}_{i=1}^B \sim \mathcal{D}\mathcal{U}\{1, \dots, T\}$ and noise $\{W^i\}_{i=1}^B \sim \mathcal{N}(0, I_d)$ with same shape as Λ_{γ_i}
- 5: $X_{t_i}^{(i)} \leftarrow \sqrt{\alpha_{t_i}} X_0^{(i)} + \sqrt{1 - \alpha_{t_i}} W^i$ ▷ forward diffusion
- 6: $s_{t_i}^*(X_{t_i}^{(i)}) \leftarrow -\frac{X_{t_i}^{(i)} - \sqrt{\alpha_{t_i}} X_0^{(i)}}{1 - \bar{\alpha}_{t_i}}$ ▷ analytic score of $p(X_{t_i}^{(i)} | X_0^{(i)})$
- 7: $\mathcal{L} \leftarrow \frac{1}{B} \sum_{i=1}^B \lambda(t_i) \|s_\theta(X_{t_i}^{(i)}, Z^i, t_i) - s_{t_i}^*(X_{t_i}^{(i)})\|^2$
- 8: Update θ using optimizer step to minimize \mathcal{L}
- 9: **end while**
- 10: **return** θ ▷ trained conditional score network

Algorithm 2 DtN measurements completion via conditional diffusion model

Require: Observed (masked) DtN measurements Λ_γ^o and its mask \mathbf{M}^o ; trained s_θ ; schedule $\{\alpha_t\}_{t=1}^T$; conditional DDPM solver 3.2;

- 1: Initialize $Y_T \sim \mathcal{N}(0, I_d)$ with same shape as Λ_γ^o , and set the condition $Z \leftarrow (\Lambda_\gamma^o, \mathbf{M}^o)$
- 2: **for** $t = T, T-1, \dots, 1$ **do**
- 3: Sample $W_t \sim \mathcal{N}(0, I)$ with same shape as Λ_γ^o
- 4: $Y_{t-1} \leftarrow \frac{1}{\sqrt{\alpha_t}} \left(Y_t + (1 - \alpha_t) s_\theta(Y_t, Z, t) + \sigma_t W_t \right)$ ▷ Conditional DDPM 3.2 update
- 5: **end for**
- 6: $\widehat{\Lambda}_\gamma \leftarrow Y_0$
- 7: **return** $\widehat{\Lambda}_\gamma$

3.3 Solve the inverse problem by data completion

We illustrate our framework for solving the EIT inverse problem in Figure 1. The figure compares three reconstruction strategies: direct reconstruction from sparse DtN measurements (first row), reconstruction from DtN measurements that are first completed and then passed to the same solver (second row), and direct reconstruction from fully sampled DtN measurements with the same solver (third row). The completed DtN measurements produced by our method are designed to be plug-and-play. Once the partially observed operator is completed to $\widehat{\Lambda}_\gamma$, it can be passed to any inverse solver that presupposes full boundary data without modification. In our experiments, rather than using a classical PDE-based inverse solver, we adopt deep learning-based inverse solvers for their stable and excellent performance. Moreover, these deep learning models offer a unified pipeline to handle both full and partial measurements, making it particularly transparent to isolate and evaluate the effect of the data-completion step.

4 Error Analysis

In this section, we provide an end-to-end error analysis for our algorithm. We are able to quantify the total variation (TV) discrepancy between the completed DtN measurements from our algorithm and that of the ground truth measurements. This section is organized as follows. In Section 4.1 we first introduce the admissible class K of conductivities of n_v -polygon shape, and its vertex parametrization v . We next show K is compact and as a consequence we can construct finitely many local charts that cover K and yield bounded parameter patches E_i . In Section 4.2, we show

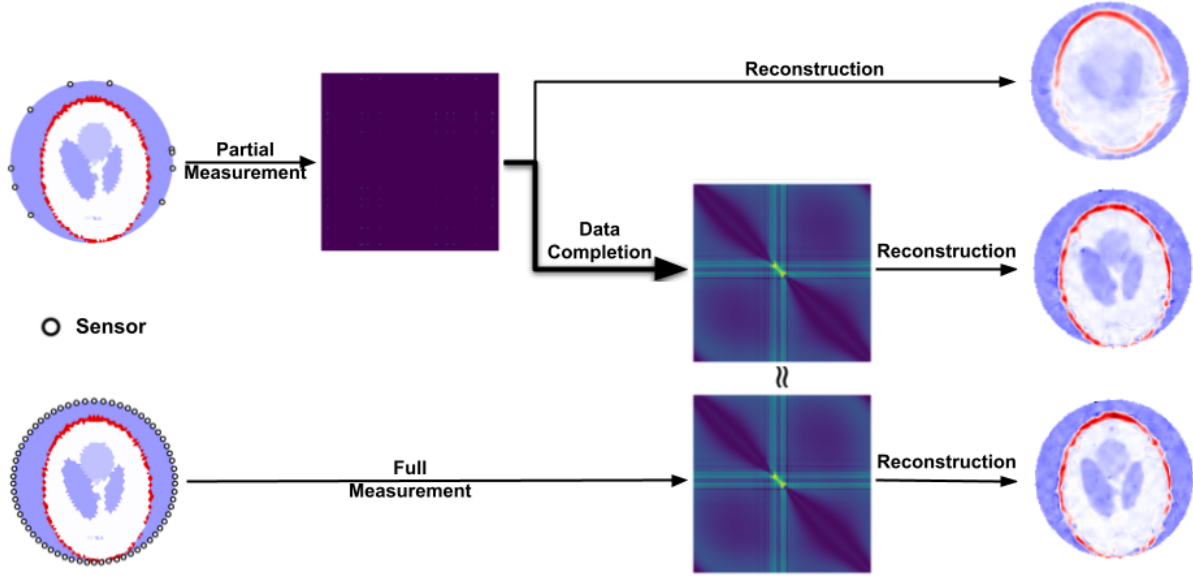


Figure 1: Three strategies of solving EIT. Direct reconstruction (**first row**) from sparse measurements yields degraded reconstruction. We propose to first complete the DtN measurements and then reconstruct (**second row**), yielding image quality close to those from a direct reconstruction from full measurements (**third row**).

that the forward map $v \mapsto \Lambda_{\gamma(v)}$ is C^1 in operator norm in each patch. In Section 4.3, we define a finite-dimensional DtN measurement map F_N and establish its patchwise Lipschitz-type stability. In Section 4.4, we leverage these patchwise stability bounds to control covering numbers for the induced measurement set. We then apply a conditional DDPM guarantee in Section 4.5 to translate these geometric controls together with a score-error assumption into the non-asymptotic DtN completion bound of Theorem 4.15. Overall, this section yields an end-to-end, non-asymptotic TV error guarantee for DtN completion over the polygonal conductivity class.

Notations. We denote by $\text{dist}(\cdot, \cdot)$ the Euclidean distance between points or subsets in \mathbb{R}^2 , and $|\cdot|$ the Euclidean norm in \mathbb{R}^2 . We also use $|E|$ to denote the Lebesgue measure of a measurable set E when no ambiguity arises. For nonempty sets $A, B \subset \mathbb{R}^2$, the Hausdorff distance is

$$d_H(A, B) := \max \left\{ \sup_{a \in A} \inf_{b \in B} \text{dist}(a, b), \sup_{b \in B} \inf_{a \in A} \text{dist}(b, a) \right\}.$$

For measurable sets $E, F \subset \mathbb{R}^2$, the symmetric difference is $E \Delta F := (E \setminus F) \cup (F \setminus E)$. We denote by $B_2(x, r) := \{y \in \mathbb{R}^2 : |y - x| \leq r\}$ the closed Euclidean ball, and by $\text{diam}(\Omega) := \sup\{|x - y| : x, y \in \Omega\}$ the diameter of a set Ω . For a simple polygon $P(v)$ with $n_v \in \mathbb{N}$ vertices $v = (v_i)_{i=0}^{n_v-1}$, we write its perimeter as

$$\text{Per}(P(v)) := \sum_{i=0}^{n_v-1} |v_{i+1} - v_i|, \quad (v_{n_v} := v_0).$$

Throughout the paper, we always assume the vertices v_i 's for a polygon $P(v)$ are ordered in the counterclockwise order. For a set $E \subset \mathbb{R}^{2n_v}$, we write $\text{conv}(E)$ for its convex hull. Finally, for a measurable set $E \subset \Omega$, χ_E denotes its indicator function.

4.1 Admissible conductivities and parametrization

Consider any integer $n_v \geq 3$, the vertex list $v = (v_0, \dots, v_{n_v-1}) \in (\mathbb{R}^2)^{n_v}$ consists pairwise distinct points with $v_{n_v} := v_0$. We define the closed polygonal chain

$$\partial P(v) := \bigcup_{i=0}^{n_v-1} [v_i, v_{i+1}], \quad [v_i, v_{i+1}] := \{(1-t)v_i + tv_{i+1} : t \in [0, 1]\}.$$

We denote by \mathcal{V}^{n_v} the set of vertex lists v such that $\partial P(v)$ is a simple (non self-intersecting) closed polygonal curve and the vertices are listed counterclockwise. For $v \in \mathcal{V}^{n_v}$, the Jordan curve theorem yields a unique bounded connected component $\text{int}(P(v))$ of $\mathbb{R}^2 \setminus \partial P(v)$; we define the (closed) n_v -gon $P(v) := \text{int}(\overline{P(v)})$. Note that the parametrization $v \mapsto P(v)$ is not injective due to the ordering of vertices (cyclic shifts and reversal).

For $v \in \mathcal{V}^{n_v}$, we denote by $\beta_i(v)$ the interior angle of $P(v)$ at the vertex v_i . We also define the polygon norm

$$\|v\|_{\text{poly}} := \max_{0 \leq i \leq n_v - 1} |v_i|, \quad \|v - w\|_{\text{poly}} := \max_{0 \leq i \leq n_v - 1} |v_i - w_i|.$$

Identifying v with an element of \mathbb{R}^{2n_v} by concatenation, we have $\|v\|_{\text{poly}} \leq \|v\|_2 \leq \sqrt{n_v} \|v\|_{\text{poly}}$.

Assumption 4.1 (Admissible polygon classes). *Fix integers $n_v \geq 3$ and constants $\beta_0 \in (0, \pi/2)$, $d_0 > 0$, $d_1 > 0$. Let $\Omega \subset \mathbb{R}^2$ be the unit disk.*

Definition 4.1 (Admissible polygon class). *Define the admissible polygon class \mathcal{A} as the set of all polygons $P = P(v)$ with their vertices $v \in \mathcal{V}^{n_v}$ such that:*

- (A1) $P \subset \Omega$ and $\text{dist}(P, \partial\Omega) \geq d_0$;
- (A2) every side length satisfies $|v_{i+1} - v_i| \geq d_1$ for all i (indices mod n_v);
- (A3) every interior angle satisfies $\beta_0 \leq \beta_i(v) \leq \pi - \beta_0$ for all i ;

Remark 4.1. *The above assumptions in Definition 4.1 imply that \mathcal{A} consists of convex polygons with nonzero side length that are away from the boundary $\partial\Omega$. These assumptions satisfy the geometric hypotheses used in Beretta and Francini, 2022, Prop. 3.3. In particular, since we only consider on convex polygon, the uniform Lipschitz boundary assumption A.1 in Beretta and Francini, 2022, Prop. 3.3 can be derived by A1–A3. We show this in the Appendix A.*

Definition 4.2 (Relaxed admissible polygon classes). *Define the relaxed class $\mathcal{A}_{1/2}$ by requiring the same conditions as above, but with strict inequalities, and the parameters are relaxed to half of their values in \mathcal{A} :*

- (A1') $P \subset \Omega$ and $\text{dist}(P, \partial\Omega) > d_0/2$;
- (A2') $|v_{i+1} - v_i| > d_1/2$ for all i (indices mod n_v);
- (A3') every interior angle satisfies $\frac{\beta_0}{2} < \beta_i(v) < \pi - \frac{\beta_0}{2}$ for all i ;

We say v is admissible if $P(v) \in \mathcal{A}$ and relaxed admissible if $P(v) \in \mathcal{A}_{1/2}$. For an admissible polygon P we consider conductivity

$$\gamma_P := 1 + (\kappa - 1)\chi_P.$$

Finally, we define the relaxed and admissible conductivity classes

$$M := \{\gamma_P : P \in \mathcal{A}_{1/2}\}, \quad K := \{\gamma_P : P \in \mathcal{A}\} \subset M.$$

Remark 4.2 (A priori data). *All constants introduced below depend only on the a priori data*

$$(\Omega, \kappa, n_v, d_0, d_1, \beta_0),$$

and are independent of the discretization level N and the number of diffusion steps T in later Section 4.3, Section 4.4 and Section 4.5.

Lemma 4.2 (Local admissibility radius). *Fix $P^* \in \mathcal{A}_{1/2}$ and let v^* be its counterclockwise ordered vertex list. Then there exists $\rho_{P^*} > 0$ such that whenever $\|v - v^*\|_{\text{poly}} < \rho_{P^*}$, the polygonal chain $\partial P(v)$ is simple and $P(v) \in \mathcal{A}_{1/2}$.*

Lemma 4.2 shows for any relaxed admissible polygon P^* , there is a small ball in the vertex space such that all polygons with vertices in the ball stays in the relaxed class. We prove Lemma 4.2 in Appendix B. The following Lemma 4.3 constructs the atlas for M , which follows the 8.1.3–8.1.5 in [Alberti et al., 2022] and is proved in Appendix C.

Lemma 4.3. *Fix $P^* \in \mathcal{A}_{1/2}$ with counterclockwise ordered vertices $v^* = (v_i^*)_{i=0}^{n_v-1}$, and let $\rho_{P^*} > 0$ be as in Lemma 4.2. Define*

$$R_{P^*} := \frac{1}{2} \min \left\{ \frac{1}{4} \min_{i \neq j} |v_i^* - v_j^*|, \text{dist}(P^*, \partial\Omega) - \frac{1}{2}d_0, \rho_{P^*} \right\} > 0,$$

$$\mathcal{O}_{P^*} := \left\{ v \in \mathbb{R}^{2n_v} : \|v - v^*\|_{\text{poly}} < R_{P^*} \right\}, \quad U_{P^*} := \left\{ \gamma_{P(v)} : v \in \mathcal{O}_{P^*} \right\},$$

and

$$\varphi_{P^*} : U_{P^*} \rightarrow \mathcal{O}_{P^*}, \quad \varphi_{P^*}(\gamma_{P(v)}) := v.$$

Then

(i) U_{P^*} is open in M with respect to the subspace topology induced by $L^1(\Omega)$.

(ii) φ_{P^*} is well-defined and is a homeomorphism from U_{P^*} onto \mathcal{O}_{P^*} .

In particular, the choice of R_{P^*} ensures (1) the neighborhood of P^* is still inside $\mathcal{A}_{1/2}$ and (2) φ is well defined and injective by ruling out the nonuniqueness caused by reordering vertex.

Lemma 4.4 (Compactness of K). *The admissible conductivity set K is compact in $L^1(\Omega)$.*

We show the compactness of the admissible set in Appendix D, which allows us to extract a finite cover of K by leveraging the local parameter neighborhoods defined in Lemma 4.3.

Lemma 4.5 (Finite patch cover and compact parameter patches). *For each $\gamma_P \in K$, let $v^P := \varphi_P(\gamma_P)$ and define the shrunken neighborhood*

$$V_P := \left\{ \gamma \in U_P : \|\varphi_P(\gamma) - v^P\|_{\text{poly}} < \frac{1}{2}R_P \right\} \subset U_P.$$

Then there exist $P_1, \dots, P_m \in \mathcal{A}$ such that

$$K \subset \bigcup_{i=1}^m V_{P_i}.$$

For each i , define the parameter patch

$$E_i := \varphi_{P_i}(K \cap \overline{V}_{P_i}) \subset \mathbb{R}^{2n_v},$$

where \overline{V}_{P_i} denotes the closure in M . Then each E_i is compact in \mathbb{R}^{2n_v} . Moreover, if we set

$$B_i := \left\{ v \in \mathbb{R}^{2n_v} : \|v - v^{P_i}\|_{\text{poly}} \leq \frac{1}{2}R_{P_i} \right\},$$

then $E_i \subset B_i \subset \varphi_{P_i}(U_{P_i})$, hence $\bigcup_{i=1}^m E_i$ is bounded and $\text{conv}(E_i) \subset \varphi_{P_i}(U_{P_i})$ for each $i = 1, \dots, m$.

The finite many parameter patches E_i will help us to quantify the complexity of DtN measurements through the local regularity of mapping from vertex to DtN measurements.

4.2 Chartwise regularity of the DtN map

To transfer low-dimensional structure from vertices to measurements, we need a quantitative regularity statement for the forward map. The regularity of mapping $v \rightarrow \Lambda_{\gamma(v)}$ has been investigated in Alberti et al. [2022], Beretta et al. [2017], Beretta and Francini [2022]. Within each chart, the DtN operator depends C^1 –smoothly on the vertex parameters. Consider

$$Y := \mathcal{L}(H^{1/2}(\partial\Omega), H^{-1/2}(\partial\Omega)), \quad \|A\|_Y := \sup_{\|f\|_{H^{1/2}(\partial\Omega)}=1} \|Af\|_{H^{-1/2}(\partial\Omega)},$$

Lemma 4.6 states the regularity statement of the forward map chartwisely.

Lemma 4.6 (C^1 -regularity of the DtN map in local coordinates). *Fix $P^* \in \mathcal{A}_{1/2}$ and let (U_{P^*}, φ_{P^*}) be the chart from Lemma 4.3. Set $\mathcal{O}_{P^*} := \varphi_{P^*}(U_{P^*}) \subset \mathbb{R}^{2n_v}$ and for $v \in \mathcal{O}_{P^*}$ define*

$$\tilde{\Lambda}_{P^*} : \mathcal{O}_{P^*} \rightarrow Y, \quad \tilde{\Lambda}_{P^*}(v) := \Lambda_{\gamma_{P^*}(v)}.$$

Then $\tilde{\Lambda}_{P^} \in C^1(\mathcal{O}_{P^*}; Y)$.*

Proof of Lemma 4.6. By Lemma 4.3, for all $v \in \mathcal{O}_{P^*}$ the polygon $P(v)$ stays in $\mathcal{A}_{1/2}$ and the counterclockwise vertex labeling is fixed in the chart. For polygonal inclusions satisfying the a priori geometric constraints, the map $v \mapsto \Lambda_{\gamma_{P^*}(v)}$ admits a shape derivative with respect to vertex perturbations, and this derivative is continuous in the operator norm of Y . This is established in the differentiability results for polygonal conductivities (see, e.g., Beretta et al., 2017, Lem. 4.4 and Cor. 4.5 and the discussion in Alberti et al., 2022, Sec. 8.1). Therefore $\tilde{\Lambda}_{P^*}$ is continuously Fréchet differentiable on \mathcal{O}_{P^*} . \square

Since $\tilde{\Lambda}_{P^*} \in C^1(\mathcal{O}_{P^*}; Y)$, the derivative $D\tilde{\Lambda}_{P^*} : \mathcal{O}_{P^*} \rightarrow \mathcal{L}(\mathbb{R}^{2n_v}, Y)$ is continuous. Moreover, $\text{conv}(E_i) \subset \mathcal{O}_{P^*}$ and $\text{conv}(E_i)$ is compact. Hence we can denote

$$M_i := \sup_{v \in \text{conv}(E_i)} \|D\tilde{\Lambda}_{P^*}(v)\|_{\text{op}} < \infty, \quad M_* := \max_{1 \leq i \leq m} M_i. \quad (12)$$

We will later use M_i and M_* to show the chartwise Lipschitz for discretized DtN measurements. For simplicity, we denote $\tilde{\Lambda}_i := \tilde{\Lambda}_{P_i}$.

4.3 Chartwise Lipschitz for the DtN measurements

We next specify the finite-dimensional representation of DtN measurements. Starting from the DtN operator $\Lambda_\gamma \in Y$, we will (i) restrict it to finite-dimensional subspaces via the R_N and obtain DtN matrix as in Equation 13, and (ii) vectorize and normalize the resulting DtN matrix to obtain a vector in Euclidean space, which is aligned to the training object in diffusion model. Combining all these yields our discretized measurement map $F_N : K \rightarrow \mathbb{R}^{d_N}$ in Equation 14.

Let $V_N^1 \subset H^{1/2}(\partial\Omega)$ and $V_N^2 \subset H^{-1/2}(\partial\Omega)$ be finite-dimensional Hilbert subspaces with inherited inner products, and denote

$$n_1 := \dim V_N^1, \quad n_2 := \dim V_N^2, \quad N := \min\{n_1, n_2\}, \quad d_N := n_1 n_2, \quad Y_N := \mathcal{L}(V_N^1, V_N^2).$$

For notational simplicity, in the sequel we focus on the square case $n_1 = n_2 = N$, which is also consistent with our numerical setup and in this case $d_N = N^2$. Let $P_N^1 : H^{1/2}(\partial\Omega) \rightarrow V_N^1$ and $P_N^2 : H^{-1/2}(\partial\Omega) \rightarrow V_N^2$ be the orthogonal projections and define

$$R_N : Y \rightarrow Y_N, \quad R_N(A) := P_N^2 A P_N^1. \quad (13)$$

Equip Y_N with the Hilbert–Schmidt norm $\|\cdot\|_{\text{HS}}$, which is independent of the choice of basis of V_N^1 and V_N^2 . Fix orthonormal bases $\{\varphi_j\}_{j=1}^{n_1}$ of V_N^1 and $\{\psi_i\}_{i=1}^{n_2}$ of V_N^2 and define the vectorization

$$\text{vec} : Y_N \rightarrow \mathbb{R}^{d_N}, \quad \text{vec}(A) := \left(\langle A\varphi_j, \psi_i \rangle_{V_N^2} \right)_{\substack{1 \leq i \leq n_2 \\ 1 \leq j \leq n_1}},$$

thus $\|\text{vec}(A)\|_2 = \|A\|_{\text{HS}}$ for all $A \in Y_N$. By introducing the finite dimensional restriction, we have following standard inequality, which records that (i) restriction and projection cannot increase operator norm, and (ii) the Hilbert–Schmidt norm of the restricted operator is controlled by the original operator norm up to a factor \sqrt{N} .

Lemma 4.7. *For any $A \in Y$,*

$$\|R_N(A)\|_{\text{op}(V_N^1 \rightarrow V_N^2)} \leq \|A\|_Y, \quad \|R_N(A)\|_{\text{HS}} \leq \sqrt{N} \|A\|_Y.$$

Proof of Lemma 4.7. Since P_N^1, P_N^2 are orthogonal projections, $\|P_N^1\| = \|P_N^2\| = 1$, hence

$$\|R_N(A)\|_{\text{op}} = \|P_N^2 A P_N^1\|_{\text{op}} \leq \|A\|_Y.$$

For the Hilbert–Schmidt norm, for any linear map $B : V_N^1 \rightarrow V_N^2$, $\|B\|_{\text{HS}} \leq \sqrt{\text{rank}(B)} \|B\|_{\text{op}}$ and $\text{rank}(R_N(A)) \leq N$, so

$$\|R_N(A)\|_{\text{HS}} \leq \sqrt{N} \|R_N(A)\|_{\text{op}} \leq \sqrt{N} \|A\|_Y.$$

□

Finally we define the discretized DtN measurement scaled by $1/\sqrt{N}$,

$$F_N : K \rightarrow \mathbb{R}^{d_N}, \quad F_N(\gamma) := \frac{1}{\sqrt{N}} \text{vec}(R_N(\Lambda_\gamma)), \quad (14)$$

and establish the Chartwise Lipschitz for F_N as follows. The $1/\sqrt{N}$ normalization rescales distances in \mathbb{R}^{d_N} , and Lipschitz constants rescale accordingly. In particular, this normalization does not change entropy exponents (rates) and only rescales accuracy parameter ε . We adopt the $1/\sqrt{N}$ normalization to absorb the discretization-induced factor \sqrt{N} , which can streamline the subsequent Lipschitz and entropy bounds. We also discuss the effect of such normalization in Appendix G.

We now combine the chartwise regularity of DtN mapping and Lemma 4.7 to conclude that, on each parameter patch E_i , the chartwise discretized forward map $G_{N,i}$ is Lipschitz in the Euclidean norm.

Lemma 4.8 (Chartwise Lipschitz for measurements). *For each i , define $G_{N,i} : E_i \rightarrow \mathbb{R}^{d_N}$ by $G_{N,i}(v) := F_N(\varphi_i^{-1}(v))$. Then $G_{N,i}$ is Lipschitz on E_i with*

$$\|G_{N,i}(v) - G_{N,i}(v')\|_2 \leq M_i \|v - v'\|_2, \quad \forall v, v' \in E_i,$$

where $M_i := \sup_{v \in \text{conv}(E_i)} \|D\tilde{\Lambda}_i(v)\|_{\text{op}} < \infty$ and independent of N .

Proof of Lemma 4.8. Using $\|\text{vec}(\cdot)\|_2 = \|\cdot\|_{\text{HS}}$ and Lemma 4.7,

$$\|G_{N,i}(v) - G_{N,i}(v')\|_2 = \frac{1}{\sqrt{N}} \|R_N(\tilde{\Lambda}_i(v) - \tilde{\Lambda}_i(v'))\|_{\text{HS}} \leq \|\tilde{\Lambda}_i(v) - \tilde{\Lambda}_i(v')\|_Y.$$

Then it suffices to show

$$\|\tilde{\Lambda}_i(v) - \tilde{\Lambda}_i(v')\|_Y \leq M_i \|v - v'\|_2.$$

To this end, we apply Fundamental theorem of calculus along the segment connecting v and v' ,

$$\tilde{\Lambda}_i(v') - \tilde{\Lambda}_i(v) = \int_0^1 D\tilde{\Lambda}_i(v + t(v' - v)) (v' - v) dt.$$

$$\|\tilde{\Lambda}_i(v) - \tilde{\Lambda}_i(v')\|_Y \leq \sup_{t \in [0,1]} \|D\tilde{\Lambda}_i(v + t(v' - v))\|_{\text{op}} \|v - v'\|_2 \leq \sup_{v \in \text{conv}(E_i)} \|D\tilde{\Lambda}_i(v)\|_{\text{op}} \|v - v'\|_2.$$

Here we apply triangle inequality for integrals and the definition of operator norm in the first inequality, and in the last inequality we use the facts that $\text{conv}(E_i) \subset \mathcal{O}_i$ and $D\tilde{\Lambda}_i$ is continuous on \mathcal{O}_i by Lemma 4.6.

□

4.4 Metric entropy and bounded support of $F_N(K)$

The diffusion convergence theorem we invoke later depends on the intrinsic complexity of the data distribution, quantified via covering numbers of its support at a prescribed resolution $\varepsilon_0 = T^{-c_{\varepsilon_0}}$, where $T \in \mathbb{N}$ is the number of diffusion steps and $c_{\varepsilon_0} > 0$ is fixed. We therefore aim to bound the metric entropy of the measurement set $F_N(K)$ with respect to the Euclidean norm $\|\cdot\|_2$.

Definition 4.3 (Covering number and metric entropy). *Let (\mathcal{X}, d) be a metric space and $S \subset \mathcal{X}$. For $\varepsilon > 0$, the covering number $\mathcal{N}_\varepsilon(S; d)$ is the smallest n such that $S \subset \bigcup_{j=1}^n B(x_j, \varepsilon)$ for some $x_1, \dots, x_n \in \mathcal{X}$, where $B(x, \varepsilon) := \{y : d(y, x) \leq \varepsilon\}$. The metric entropy is defined as $\log \mathcal{N}_\varepsilon(S; d)$.*

The following lemma shows that an L -Lipschitz map does not increase covering numbers after rescaling the covering radius.

Lemma 4.9 (Coverings under Lipschitz maps). *Let $(\mathcal{X}, d_{\mathcal{X}})$ and $(\mathcal{Z}, d_{\mathcal{Z}})$ be metric spaces. If $f : \mathcal{X} \rightarrow \mathcal{Z}$ is L -Lipschitz, then for any $S \subset \mathcal{X}$ and $\varepsilon > 0$,*

$$\mathcal{N}_\varepsilon(f(S); d_{\mathcal{Z}}) \leq \mathcal{N}_{\varepsilon/L}(S; d_{\mathcal{X}}).$$

Proof of Lemma 4.9. Let $\{x_j\}_{j=1}^n$ be an ε/L -net of S in $d_{\mathcal{X}}$ with $n = \mathcal{N}_{\varepsilon/L}(S; d_{\mathcal{X}})$, so $S \subset \bigcup_{j=1}^n B_{\mathcal{X}}(x_j, \varepsilon/L)$. For any $z = f(s) \in f(S)$ choose j with $d_{\mathcal{X}}(s, x_j) \leq \varepsilon/L$. Then $d_{\mathcal{Z}}(z, f(x_j)) \leq Ld_{\mathcal{X}}(s, x_j) \leq \varepsilon$. This implies that $\{f(x_j)\}$ is an ε -net of $f(S)$, and as a consequence, the covering number of $f(S)$ is no greater than n . □

Remark 4.3. *If a map is rescaled by a scalar factor $a > 0$ (e.g. $a = 1/\sqrt{N}$ in the definition of F_N), then af is (aL) -Lipschitz whenever f is L -Lipschitz. Thus Lemma 4.9 shows that such normalizations only rescale the covering radius (hence modify constants), and do not affect the exponent in the metric-entropy bounds.*

We also need a volumetric covering bound in \mathbb{R}^{2n_v} , since an n_v -gon in \mathbb{R}^2 is parameterized by its n_v ordered vertices in \mathbb{R}^2 , i.e. $v \in \mathbb{R}^{2n_v}$.

Lemma 4.10 (Volumetric covering in \mathbb{R}^{2n_v}). *There exists an absolute constant $C_{\text{vol}} > 0$ such that the following holds. If $E \subset \mathbb{R}^{2n_v}$ satisfies $E \subset B_2(0, R)$ for some $R > 0$, then for every $\delta > 0$,*

$$\mathcal{N}_\delta(E; \|\cdot\|_2) \leq \max \left\{ 1, \left(\frac{C_{\text{vol}} R}{\delta} \right)^{2n_v} \right\}.$$

Remark 4.4. *Applying Lemma 4.10 to a globally rescaled set aE simply replaces R by aR , where $a > 0$ is an arbitrary constant. Consequently, the $1/\sqrt{N}$ normalization in F_N can only enter through prefactors such as $C_{\text{vol}}R$ (or Lipschitz constants), while the exponent $2n_v$ remains unchanged.*

We now bound (i) the metric entropy of $F_N(K)$ and (ii) a uniform radius bound for its support. The proof covers K by finitely many patches, uses Lipschitz bounds for the chartwise measurement maps, and applies a volumetric covering estimate in \mathbb{R}^{2n_v} .

Lemma 4.11 (Uniform boundedness of DtN operator on K). *Define $r_K := \sup_{\gamma \in K} \|\Lambda_\gamma\|_Y$. Then $r_K < \infty$.*

Proof of Lemma 4.11. On K , γ is uniformly elliptic and bounded by $\min\{1, \kappa\} \leq \gamma(x) \leq \max\{1, \kappa\}$. Standard energy estimates for elliptic boundary value problems imply that $\|\Lambda_\gamma\|_Y$ is uniformly bounded over $\gamma \in K$, hence $r_K < \infty$ [Evans, 2022]. \square

We could now define the maximum radius for all local coordinate patches

$$R_* := \max_{1 \leq i \leq m} \sup_{v \in E_i} \|v\|_2 < \infty. \quad (15)$$

Theorem 4.12 (Metric entropy and bounded support of discretized DtN measurements). *Consider $F_N : K \rightarrow \mathbb{R}^{d_N}$ in Equation 14. Fix $c_{\varepsilon_0} > 0$ and for all $T \geq 2$ set $\varepsilon_0 := T^{-c_{\varepsilon_0}}$. Let $C_{\text{vol}} > 0$ be as in Lemma 4.10. Then for all $T \geq 2$,*

$$\log \mathcal{N}_{\varepsilon_0}(F_N(K); \|\cdot\|_2) \leq C_F \log T, \quad (16)$$

where one may take

$$C_F := 2n_v c_{\varepsilon_0} + \frac{\log m + 2n_v \log(C_{\text{vol}} R_* M_*)}{\log 2}. \quad (17)$$

Here m and R_* are as in Lemma 4.5, M_i is the Lipschitz constant of $G_{N,i}$ given in Lemma 4.8, and $M_* := \max_{1 \leq i \leq m} M_i$. Moreover, $F_N(K)$ is bounded in \mathbb{R}^{d_N} and satisfies

$$\sup_{\gamma \in K} \|F_N(\gamma)\|_2 \leq r_K,$$

where r_K is the finite constant from Lemma 4.11.

Proof. By Lemma 4.5, $K \subset \bigcup_{i=1}^m V_{P_i}$, hence

$$F_N(K) \subset \bigcup_{i=1}^m F_N(K \cap \overline{V}_{P_i}) = \bigcup_{i=1}^m G_{N,i}(E_i),$$

where $E_i \subset \mathbb{R}^{2n_v}$ is the i -th parameter patch and $G_{N,i} : E_i \rightarrow \mathbb{R}^{d_N}$ is defined in Lemma 4.8. Therefore for any $\varepsilon > 0$,

$$\mathcal{N}_\varepsilon(F_N(K); \|\cdot\|_2) \leq \sum_{i=1}^m \mathcal{N}_\varepsilon(G_{N,i}(E_i); \|\cdot\|_2) \leq \sum_{i=1}^m \mathcal{N}_{\varepsilon/M_i}(E_i; \|\cdot\|_2), \quad (18)$$

where the last inequality follows from Lemma 4.8 and Lemma 4.9.

Each $E_i \subset \mathbb{R}^{2n_v}$ is bounded and satisfies $E_i \subset B_2(0, R_*)$ by definition of R_* . Applying Lemma 4.10 gives, for every $\varepsilon > 0$,

$$\mathcal{N}_{\varepsilon/M_i}(E_i; \|\cdot\|_2) \leq \max \left\{ 1, \left(\frac{C_{\text{vol}} R_* M_i}{\varepsilon} \right)^{2n_v} \right\}.$$

Hence,

$$\mathcal{N}_\varepsilon(F_N(K); \|\cdot\|_2) \leq m \max \left\{ 1, \left(\frac{C_{\text{vol}} R_* M_*}{\varepsilon} \right)^{2n_v} \right\}.$$

Taking $\varepsilon = \varepsilon_0 = T^{-c_{\varepsilon_0}}$ yields

$$\log \mathcal{N}_{\varepsilon_0}(F_N(K)) \leq \log m + 2n_v \log(C_{\text{vol}} R_* M_*) + 2n_v c_{\varepsilon_0} \log T.$$

Since $T \geq 2$, the additive constant satisfies

$$\log m + 2n_v \log(C_{\text{vol}} R_* M_*) \leq \frac{\log m + 2n_v \log(C_{\text{vol}} R_* M_*)}{\log 2} \log T,$$

which gives Equation 16 with C_F in Equation 17.

We now show a uniform radius bound for $F_N(K)$. Using $\|F_N(\gamma)\|_2 = \frac{1}{\sqrt{N}} \|R_N(\Lambda_\gamma)\|_{\text{HS}}$, Lemma 4.7, and Lemma 4.11,

$$\|F_N(\gamma)\|_2 \leq \|\Lambda_\gamma\|_Y \leq r_K.$$

Taking the supremum over $\gamma \in K$ completes the proof. \square

4.5 Convergence guarantee for diffusion completion

Consider the (scaled) full discretized DtN measurement vector

$$X_0 := F_N(\gamma) \in \mathbb{R}^{d_N},$$

and the corresponding observed data

$$Z := (\mathbf{M}, \mathbf{M} \odot X_0) \in \{0, 1\}^{d_N} \times \mathbb{R}^{d_N}.$$

Note that F_N includes the normalization $1/\sqrt{N}$ in Equation 14.

We recall the unconditional result of Liang et al. [2025, Thm. 2] and will apply it to each conditional distribution $p_{X_0|Z=z}$ by treating z as a fixed parameter.

Lemma 4.13 (Unconditional DDPM convergence under low intrinsic complexity (Liang et al., 2025, Thm. 2)). *Let $X_0 \sim p_{\text{data}}$ be a distribution on \mathbb{R}^d satisfying Assumptions 1–3 of Liang et al. [2025] (intrinsic dimension k quantified by metric entropy at $\epsilon_0 = T^{-c_{\epsilon_0}}$, bounded support with radius $R = T^{c_R}$, and averaged ℓ_2 score error $\varepsilon_{\text{score}}$). Then the DDPM sampler satisfies*

$$\text{TV}(p_{X_1}, p_{Y_1}) \lesssim \frac{k \log^3 T}{T} + \varepsilon_{\text{score}} \sqrt{\log T}. \quad (19)$$

In our polygonal EIT setting, the natural parameter dimension is $k = 2n_v$ (ordered vertices in \mathbb{R}^2). The metric entropy bound for intrinsic dimension and the boundedness of support have been verified in Theorem 4.12, which depends on the assumptions for admissible polygons. We assume the conditional score estimation error as follows.

Assumption 4.14 (ℓ_2 conditional score error). *There exists $\varepsilon_{\text{score}} \geq 0$ such that for Z -almost every z ,*

$$\frac{1}{T} \sum_{t=1}^T \mathbb{E} \left[\|s_\theta(X_t, z, t) - s_t^*(X_t, z)\|_2^2 \mid Z = z \right] \leq \varepsilon_{\text{score}}^2.$$

Remark 4.5. Assumption 4.14 abstracts the error incurred by learning the conditional score from data using a neural network. Providing a rigorous, nonasymptotic bound for $\varepsilon_{\text{score}}$ is a nontrivial learning-theoretic problem and typically depends on the model class, training procedure, and regularity properties of the target conditional score. In this paper we follow the common approach in the diffusion convergence literature and treat $\varepsilon_{\text{score}}$ as an exogenous accuracy parameter, as in [Chen et al., 2023, Benton et al., 2023, Liang et al., 2025].

With conditional score error estimation in Assumption 4.14, we verify the assumptions of Liang et al. [2025, Thm. 2] for each conditional law $p_{X_0|Z=z}$ and obtain the following guarantee.

Theorem 4.15 (Conditional DDPM completion error in TV). *Consider the set of full DtN measurements from all admissible conductivities $F_N(K) \subset \mathbb{R}^{d_N}$, and let $\epsilon_0 := T^{-c_{\epsilon_0}}$ with $c_{\epsilon_0} > 0$ as in Liang et al., 2025, Assumption 1. Assume furthermore that Assumption 4.14 holds. Then for Z -almost every z , the conditional DDPM sampler produces $Y_1 \mid Z = z$ whose law satisfies*

$$\text{TV}(p_{X_1|Z=z}, p_{Y_1|Z=z}) \lesssim \frac{2n_v \log^3 T}{T} + \varepsilon_{\text{score}} \sqrt{\log T}. \quad (20)$$

Proof. Fix z such that Assumption 4.14 holds. Since $X_0 \in F_N(K)$ almost surely, it follows that $\text{supp}(p_{X_0|Z=z}) \subset F_N(K)$. Consequently, for any $\epsilon > 0$,

$$\mathcal{N}_\epsilon(\text{supp}(p_{X_0|Z=z}); \|\cdot\|_2) \leq \mathcal{N}_\epsilon(F_N(K); \|\cdot\|_2), \quad \sup_{x \in \text{supp}(p_{X_0|Z=z})} \|x\|_2 \leq r_K.$$

Taking $\epsilon = \epsilon_0$ yields

$$\log \mathcal{N}_{\epsilon_0}(\text{supp}(p_{X_0|Z=z})) \leq C_F \log T,$$

by metric entropy bound from Theorem 4.12. Therefore Liang et al., 2025, Assumption 1 holds for $p_{X_0|Z=z}$ with intrinsic dimension $k = 2n_v$ and constant $C_{\text{cover}} := C_F/(2n_v)$. The radius bound from Theorem 4.12 verifies Liang et al., 2025, Assumption 2, since r_K does not depend on T and we can choose $c_R \geq \log_2 r_K$ such that $r_K \leq T^{c_R}$ for $T \geq 2$.

Assumption 4.14 is the conditional analogue of Liang et al., 2025, Assumption 3. For each fixed z , the conditional DDPM is an unconditional DDPM on \mathbb{R}^{d_N} with data law $p_{X_0|Z=z}$. Applying Lemma 4.13 to $p_{X_0|Z=z}$ yields Equation 20. \square

Remark 4.6 (Why the conclusion is stated at time $t = 1$). *The TV guarantee above compares $p_{X_1|Z=z}$ and $p_{Y_1|Z=z}$, consistent with Liang et al., 2025, Thm. 2. For data distributions supported on low-dimensional sets in \mathbb{R}^d , a TV guarantee directly for $p_{X_0|Z=z}$ is generally impossible against any absolutely continuous sampler output, due to mutual singularity.*

The ambient dimension of the measurement vector is $d_N = N^2$, whereas the admissible family $F_N(K)$ is parameterized by only $2n_v$ real parameters (ordered vertices in \mathbb{R}^2). This low-dimensional structure is reflected in the metric-entropy bound Equation 16: after passing to local coordinates, the forward map is Lipschitz on each patch, so the covering numbers of $F_N(K)$ are controlled by volumetric coverings in \mathbb{R}^{2n_v} , yielding the power $2n_v$ in the covering-number bound.

5 Numerical Experiments

In this section, we evaluate the proposed method against baseline approaches on two tasks: (i) completing full DtN measurements from randomly sampled sparse measurements, and (ii) reconstructing EIT conductivities from sparse measurements. The details of the experimental setup and model training are provided in Sections 5.1 and 5.2, while the testing results are reported in Sections 5.3 and 5.4.

5.1 Data generation

Discretizations We consider the unit disk as the computational domain Ω , which is discretized over a conforming triangular mesh (see Figure 2). This results in $N_T = 1324$ interior nodal points, $N_B = 128$ boundary nodal points, and 2774 triangular elements. The elliptic PDE Equation 1 is then solved using the finite element method (FEM) with P1 elements. Consequently, the DtN measurement matrix has size 128×128 , while the conductivity γ is discretized into a vector of length 2774 at the centroids of all elements. To facilitate the use of conductivity data in deep learning models, γ is zero-padded and extended to a function on the square $[-1, 1] \times [-1, 1]$, and then discretized over a 128×128 grid via linear interpolation, as shown in Figure 2.

Conductivity distributions We consider two different distributions of conductivity throughout this section, which are defined as follows.

- **Disks:** This dataset consists of conductivities over a unit disk Ω with unit background value, together with constant values over a few circular inclusions. In particular, the conductivities are defined as the following.

$$\gamma(x) = 1 + \sum_{i=1}^n (c_i - 1) \mathbf{1}_{\{\|x-x_i\|_2 \leq r_i\}}(x), \quad x \in \Omega,$$

where $n \in \{2, 3, 4, 5\}$, and the inclusion centers $x_i \in \Omega$, radii r_i , and contrasts c_i vary across samples. For each fixed n , we independently draw radii $r_i \sim \mathcal{U}[0.2, 0.4]$, contrasts $c_i \sim \mathcal{U}[2, 8]$, and centers x_i uniformly over Ω . We use rejection sampling to ensure that the inclusions are fully contained within Ω and mutually disjoint. That is,

$$\text{dist}(x_i, \partial\Omega) > r_i \quad \text{for all } i, \quad \text{and} \quad \|x_i - x_j\|_2 > r_i + r_j \quad \text{for all } i \neq j.$$

For each $n \in \{2, 3, 4, 5\}$, 500 admissible training samples and 100 admissible test samples are generated, yielding a total of 2000 training and 400 test conductivities.

- **Shepp–Logan Phantom:** This dataset is based on Shepp and Logan [1974], a standard benchmark in medical imaging that consists of piecewise constant functions that model human skulls, ventricles and tumors. Our code follows the setup in Chung [2020].

Examples of conductivities in each dataset can be found in the leftmost columns of Figure 7 and Figure 9 respectively.

Normalization of the DtN measurement The DtN measurement Λ_γ exhibits strong heterogeneity between diagonal and off-diagonal entries, as the off-diagonal entries are fast-decaying for any L^∞ coefficient γ [Bebendorf and Hackbusch, 2003, Bechtel and Ouhabaz, 2024]. Furthermore, the ill-posedness of the Calderón problem suggests that the difference between two measurements Λ_{γ_1} and Λ_{γ_2} is highly insensitive to their corresponding conductivity differences. As a consequence, all DtN measurements are similar to those of the background (unit) conductivity [Alessandrini, 1988]. Such similarity in the data causes a significant challenge in training effective deep learning models. To this end, we normalize each DtN measurement by that of the background (unit) conductivity. The normalized DtN

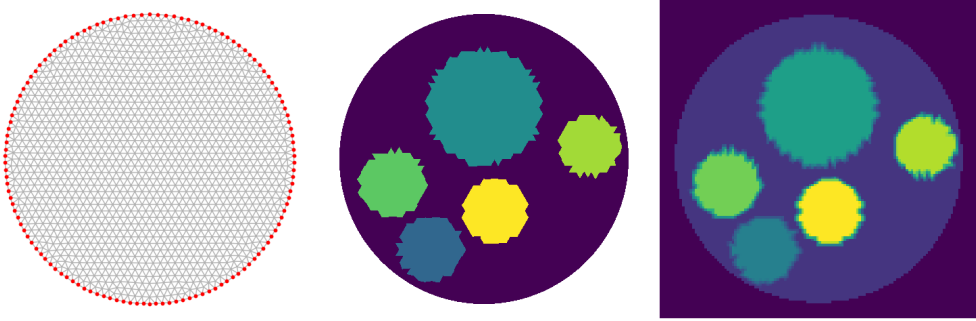


Figure 2: Discretization of conductivity γ . **Left:** Triangular mesh over the unit disk where red boundary points mark candidate sensor locations. **Middle:** A conductivity over the triangular mesh from the Disk distribution. **Right:** The same conductivity converted to a uniform 128×128 Cartesian grid on $[-1, 1] \times [-1, 1]$ with zero padding.

measurement is defined as the elementwise (Hadamard) ratio $\bar{\Lambda}_\gamma := \Lambda_\gamma \oslash \Lambda_1$. All models are trained and evaluated on the normalized DtN measurement $\bar{\Lambda}_\gamma$. As illustrated in Figure 3, raw DtN measurements are visually similar across distinct conductivities, whereas their normalized version reveals discriminative patterns.

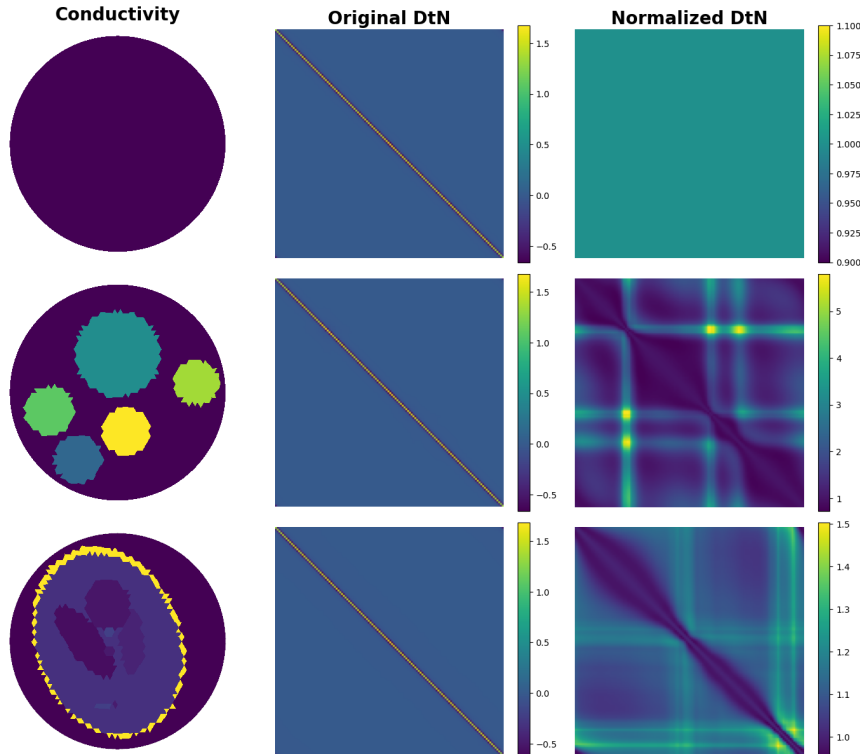


Figure 3: Normalization of DtN measurements. **Left column:** conductivity fields (top: background; middle: disks; bottom: Shepp–Logan phantom). **Middle column:** raw DtN matrices computed from the corresponding conductivities. **Right column:** normalized DtN matrices produced by our preprocessing step.

Measurement configurations Two types of mask matrices are considered in our numerical experiments.

- **Principal submatrix:** Sources and receivers are placed on a fixed number of boundary nodes that are chosen uniformly at random. In this case, the mask matrix \mathbf{M}_s is a principal submatrix, i.e.

$$(\mathbf{M}_s)_{ij} = \begin{cases} 1, & i \in \mathcal{S} \text{ and } j \in \mathcal{S}, \\ 0, & \text{otherwise.} \end{cases}$$

where an index set $\mathcal{S} \subset [N_B]$ is drawn uniformly at random without replacement. The total number of boundary nodes $|\mathcal{S}| = \lfloor \sqrt{s} N_B \rfloor$ is determined by the sampling rate $s \in (0, 1)$.

- **Random:** Each entry of Λ_γ is observed independently with probability s as in Bui-Thanh et al. [2022]. The mask \mathbf{M}_s is therefore a Bernoulli random matrix with parameter s , i.e.,

$$(\mathbf{M}_s)_{ij} = \begin{cases} 1, & \text{w.p. } s, \\ 0, & \text{w.p. } 1 - s. \end{cases}$$

Examples of both types of mask matrices are plotted in Figure 5.

Noise injection To investigate the robustness of our methods, we apply a noise pattern considered in Borcea et al. [2013], which is similar to multiplicative noise, to both training and testing measurements.

$$\Lambda_\gamma^{\text{Noisy}} = \Lambda_\gamma + \sigma_{\text{noise}} \Lambda_1 \odot \mathcal{E},$$

where Λ_1 is the background DtN measurement, $\sigma_{\text{noise}} \in (0, 1)$ is the strength of noise, and $\mathcal{E} \in \mathbb{R}^{N_B \times N_B}$ is a random matrix whose entries are independently drawn from the standard normal distribution. We consider $\sigma_{\text{noise}} = 0.05(5\%)$ in our experiments, and inject noise to Λ_γ first and then apply the normalization to obtain $\bar{\Lambda}_\gamma$.

5.2 Implementation details

We evaluate the proposed method through two stages: data completion in Section 5.3 and conductivity reconstruction in Section 5.4. In the data completion stage, we compare our method with the hierarchical completion baseline introduced in Bui-Thanh et al. [2022]. In the conductivity reconstruction stage, we adopt IAE-Net, an efficient neural operator introduced in Ong et al. [2022], which achieves excellent accuracy on forward and inverse PDE operator learning tasks. To demonstrate the effectiveness of our proposed method, we compare the results of three inverse problem solving strategies illustrated in Figure 1: (i) *direct reconstruction from sparse measurements*; (ii) *data completion followed by reconstruction*, where the data completion part is implemented by our diffusion model or by the hierarchical matrix completion; and (iii) *direct reconstruction from full measurements*, which sets the best achievable accuracy for the specified inverse solver (e.g. IAE-Net). We next details the implementations of our diffusion completion model in Section 5.2, the hierarchical matrix completion baseline, and the IAE-Net inverse solver, along with the evaluation metrics.

5.2.1 Data completion methods

Diffusion model implementation We adopt the Elucidated Diffusion Model (EDM) framework [Karras et al., 2022] with the preconditioned denoising network D_θ , which can be interpreted as a reparameterization of the score functions studied in Song et al. [2020b], Ho et al. [2020]. The denoiser network $D_\theta(x, \sigma)$ in Karras et al. [2022] predicts a clean DtN measurement x_0 from a perturbed input $x = x_0 + \sigma \varepsilon$, where $\varepsilon \sim \mathcal{N}(0, I)$ and σ is the noise level. For training, we use the same loss function and noise-level sampling strategy as in Karras et al. [2022], and train the model on normalized DtN measurement data. The denoiser D_θ is implemented as a 2D U-Net [Ronneberger et al., 2015], where each DtN matrix is treated as a single-channel image. The network has a base width of 128, includes two residual blocks at each resolution level, and performs dyadic downsampling and upsampling by a factor of 2, repeated three times, with an encoder-decoder symmetric structure and skip connections. Each residual block consists of 3×3 convolutions, normalization, and SiLU activations. The scalar noise level σ is encoded using a Fourier embedding and injected into the residual blocks via affine modulation. Attention mechanisms are applied only in the bottleneck layer. Optimization is carried out with AdamW [Loshchilov and Hutter, 2017] using a learning rate of 10^{-4} , an exponential moving average of model parameters with decay 0.999, and a batch size of 32. Unless otherwise specified, all remaining EDM hyperparameters and conventions follow Karras et al. [2022].

Baseline model: hierarchical matrix completion We consider the hierarchical matrix completion method in Bui-Thanh et al. [2022] as a baseline for completing DtN measurements. This method exploits the hierarchical off-diagonally low-rank structure of the DtN measurement matrix [Bebendorf and Hackbusch, 2003, Ballani and Kressner, 2017] and employs standard matrix completion methods [Recht, 2011]. Concretely, the DtN matrix is divided into a hierarchical tree of diagonal blocks and off-diagonal blocks as shown in Figure 4. To apply matrix completion globally, a corresponding hierarchical masking matrix needs to be considered for this method. In particular, it is assumed that the observed EIT measurements consist of all data on the diagonal blocks and partial data that are sampled uniformly at random over all off-diagonal blocks. See Figure 6 for the global masking matrix considered in such hierarchical setting. Specifically, we implement a three-level decomposition of the measurement matrix, which leads to in total

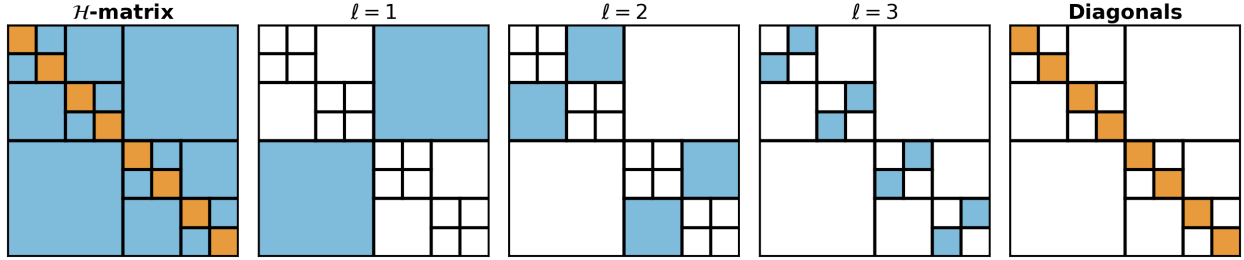


Figure 4: Hierarchical partition with level 3. *Diagonal blocks* are colored in orange, and *off-diagonal blocks* are colored in blue.

eight diagonal blocks and fourteen off-diagonal blocks. The matrix completion algorithm is applied in parallel to each of the off-diagonal blocks to obtain the completed data, which are then assembled together to form the completed measurement matrix. In particular, consider an arbitrary off-diagonal block $\Lambda_\gamma^l \in \mathbb{R}^{\frac{N_B}{2^l} \times \frac{N_B}{2^l}}$ at level $l = 1, 2, 3$ and a random mask \mathbf{M}_s^l of the same size, the matrix completion algorithm outputs a solution to the following constrained nuclear norm optimization problem

$$\widehat{\Lambda}_\gamma^l = \arg \min_X \|X\|_* \quad \text{subject to} \quad \mathbf{M}_s^l \odot X = \mathbf{M}_s^l \odot \Lambda_\gamma^l, \quad X \in \mathbb{R}^{\frac{N_B}{2^l} \times \frac{N_B}{2^l}}. \quad (21)$$

where $\|\cdot\|_*$ denotes the matrix nuclear norm. The above minimization problem admits a unique solution if the sampling rate in the random mask \mathbf{M}_s^l is sufficiently large. We implement the nuclear optimization Equation 21 with the MOSEK solver from the CVXPY package.

5.2.2 Inverse problem solver

We employ the neural operator IAE-Net [Ong et al., 2022] as our inverse solver, for its excellent accuracy across various PDE forward and inverse operator learning tasks. Two IAE-Net models are trained separately on clean data to serve as a full-data solver and sparse-data solver respectively. In particular, the full-data solver is trained to learn the operator $\mathcal{G} : \bar{\Lambda}_\gamma \mapsto \gamma$ that maps the full DtN measurements to target conductivity field, while the sparse-data solver approximates $\mathcal{G}_{\text{masked}} : \bar{\Lambda}_\gamma^0 \mapsto \gamma$, where $\bar{\Lambda}_\gamma^0 = \mathbf{M}_s \odot \bar{\Lambda}_\gamma$. Specifically, \mathbf{M}_s is a principal submatrix mask resampled independently at each training iteration, enabling the model to adapt to diverse sparse-measurement patterns.

Both IAE-Net models are configured with 32 modes and a stack of IAE blocks, using four blocks for the Disks dataset and two for the Shepp–Logan dataset. Training minimizes the mean-squared error between predicted and ground-truth conductivities, optimized with Adam and weight decay 10^{-4} . The learning rate follows a reduce-on-plateau schedule (factor 0.5, patience 20), with early stopping after 40 stagnant epochs and a maximum of 300 epochs. The initial learning rate is 10^{-2} for the Disks dataset and 10^{-3} for the Shepp–Logan dataset.

5.2.3 Evaluation metrics

In order to compare the proposed data completion method with the baseline, we consider the following evaluation metrics. These metrics quantify the fidelity of the completed DtN data and the accuracy of reconstructed conductivity respectively.

DtN data completion error A core objective of our framework is to accurately reconstruct the missing DtN measurements in Λ_γ^0 . We measure reconstruction quality using the normalized relative Frobenius error:

$$\text{RE}(\widehat{\Lambda}_\gamma) = \frac{\|\widehat{\Lambda}_\gamma - \bar{\Lambda}_\gamma\|_F}{\|\bar{\Lambda}_\gamma\|_F}, \quad (22)$$

where $\bar{\Lambda}_\gamma$ denotes the normalized ground-truth DtN measurements and $\widehat{\Lambda}_\gamma$ is the completed normalized DtN measurements.

Conductivity reconstruction error Note that the conductivity is defined on unit disk $\Omega \subset [-1, 1]^2$ and padded zeros outside Ω . We only measure the errors within Ω . In particular, let $\{x_i\}_{i=1}^{128}$ and $\{y_j\}_{j=1}^{128}$ be the uniform grid coordinates on $[-1, 1]$ and define

$$\Omega_{\text{grid}} = \{(i, j) : x_i^2 + y_j^2 \leq 1\}, \quad N_\Omega = |\Omega_{\text{grid}}|.$$

For a given neural network prediction $\hat{\gamma}$, we measure its relative ℓ_2 error and the mean absolute error with respect to the ground truth γ restricted to Ω :

$$\text{RE}(\hat{\gamma}) = \frac{\sqrt{\sum_{(i,j) \in \Omega_{\text{grid}}} (\hat{\gamma}_{i,j} - \gamma_{i,j})^2}}{\sqrt{\sum_{(i,j) \in \Omega_{\text{grid}}} \gamma_{i,j}^2}}, \quad \text{MAE}(\hat{\gamma}) = \frac{1}{N_{\Omega}} \sum_{(i,j) \in \Omega_{\text{grid}}} |\hat{\gamma}_{i,j} - \gamma_{i,j}|.$$

In addition, we also introduce structural similarity (SSIM) for evaluating conductivity reconstruction. SSIM quantifies perceptual similarity by jointly comparing local luminance, contrast, and structure, thereby capturing preservation of geometry and edges more faithfully than pixel-wise metrics such as ℓ_2 error or MAE. Given two conductivities γ_1, γ_2 , the local structural similarity at pixel p is

$$\text{SSIM}_w(\gamma_1, \gamma_2) = \frac{(2\mu_1(p)\mu_2(p) + C_1)(2\sigma_{12}(p) + C_2)}{(\mu_1(p)^2 + \mu_2(p)^2 + C_1)(\sigma_1^2(p) + \sigma_2^2(p) + C_2)},$$

where μ_1, μ_2 are local means, σ_1^2, σ_2^2 local variances, and σ_{12} the local covariance computed with a sliding window w . The reported image-level SSIM is the mean of these local SSIM:

$$\text{SSIM}(\gamma_1, \gamma_2) = \frac{1}{|\mathcal{W}|} \sum_{w \in \mathcal{W}} \text{SSIM}_w(\gamma_1, \gamma_2),$$

with \mathcal{W} the set of all sliding windows. In our implementation, we compute SSIM using the `scikit-image` package [Van der Walt et al., 2014] with default settings.

5.3 Results for data completion

We compare our diffusion-based data completion to the hierarchical matrix completion method as in Bui-Thanh et al. [2022]. Since identical matrix completion algorithms Equation 21 are applied to all off-diagonal blocks with the same sampling rate, it is equivalent to compare data completion results restricted to a single off-diagonal block. To this end, we implement our method and matrix completion over the upper right off-diagonal block at the first level in the subsequent subsection, and present the accuracy of data completion with various sampling rates from $s = 1\%$ to $s = 30\%$.

Off-diagonal block completion We evaluate both methods on the upper-right off-diagonal block of the DtN matrix, which has size 64×64 and a numerical rank of 10. We test the diffusion completion method under principal submatrix masking with sampling rate $s = 1\%$, and matrix completion method under both principal submatrix masking and random masking with various sampling rates, see Figure 5. We find that the diffusion model is able to reconstruct the off-diagonal block of DtN matrix within a relative error of 0.9% with only 1% of observed data. In comparison, matrix completion fails to find any missing data under the same setting. This is because the masked measurement is already of low rank when the sampling rate $s = 1\%$ is low, and thus becomes a solution to Equation 21. Consequently, no missing data can be obtained from the nuclear norm optimization. We further test matrix completion under random masking with different sampling rate $s = 1\%, 15\%$ and 30% . We observe that the same issue persists with low sampling rate 1%. An unsatisfactory reconstruction can be achieved with larger sampling rate $s = 15\%$ with relative error 8.2%. When the random sampling rate is raised to $s = 30\%$, a competitive reconstruction result with relative error 1.0% is achieved. Overall, Figure 5 illustrates that a learned distributional prior (diffusion) can interpolate across ultra-sparse observations, while low-rank matrix completion requires denser, randomly distributed observations to perform well.

5.4 Results for inverse problem solving

In this section, we investigate the effectiveness of inverse problem solving with completed measurement data from the proposed method in Sections 5.4.1 and 5.4.2, respectively. Given sparse DtN measurements, we evaluate the reconstruction performance of different methods, including **i**) a direct reconstruction by a sparse-data solver; **ii**) a level-3 hierarchical matrix completion followed by a full-data solver; and **iii**) a diffusion completion followed by the same full-data solver. Note that even with the ground truth data, the inherent nonlinearity and ill-posedness of the EIT problem can lead to non-negligible reconstruction errors, particularly under noisy or sparse measurement conditions. To this end, the output of a full-data solver with full data represents the best possible reconstruction from a specific inverse problem solver. We report this reconstruction as a reference to demonstrate the effectiveness of the aforementioned methods.

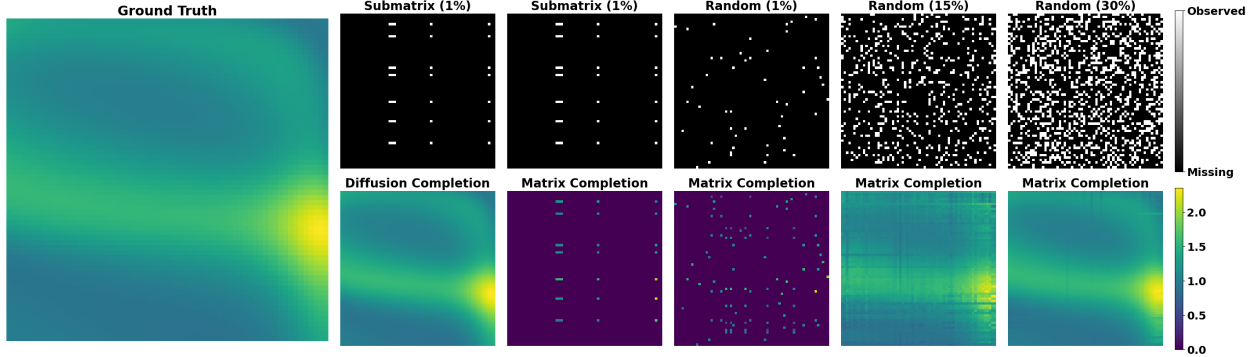


Figure 5: Diffusion completion versus matrix completion on an off-diagonal block under different masking patterns and sampling rate. *Note that the matrix-completion baseline is only applied to off-diagonal blocks, where low-rank structure is expected, whereas our diffusion model is applied to the whole matrix and presents the off-block in this plot* **Left:** ground truth (normalized) upper-right block of DtN matrix. **Right, top row:** masking matrices with sampling rate $s = 1\%$, $s = 15\%$ and $s = 30\%$. **Right, bottom row:** corresponding reconstructions under the masks shown above. The diffusion model (first column) achieves high-quality reconstruction under the submatrix masking even at an extremely low sampling rate $s = 1\%$ with relative error (RE) 0.9%. In contrast, matrix completion fails at $s = 1\%$ under both submatrix and random masking (second and third columns). Matrix completion requires substantially higher random sampling rates (fourth and fifth columns) to achieve comparable accuracy, reaching RE 8.2% at $s = 15\%$ and RE 1.0% at $s = 30\%$. In contrast, our diffusion model performs completion over the entire DtN matrix.

Specifically, to obtain reasonable reconstructions by matrix completion, we consider a higher sampling rate (15%) in each off-diagonal block. This results in a global hierarchical random mask with an overall sampling rate of 25.625%. For diffusion completion and direct sparse solver, a more practical principal submatrix masking is considered with sampling rate 1%. These two different masking matrices are plotted in Figure 6.

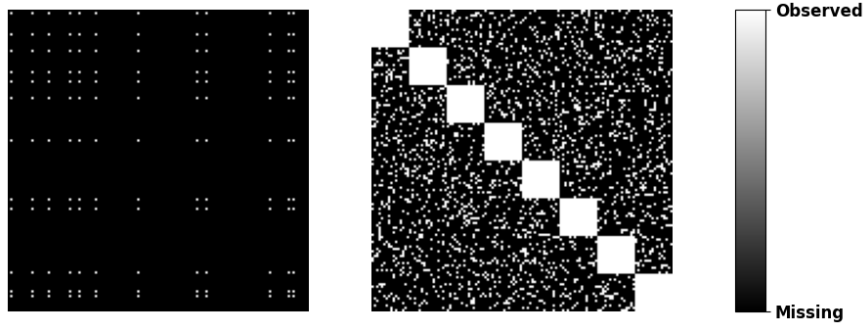


Figure 6: Global masking matrices. **Left:** The mask matrix used for diffusion completion and the sparse-data solver. This mask consists of nonzero values over a principal submatrix with sampling rate $s = 1\%$. **Right:** The hierarchical masking matrix with level $l = 3$. In this case, all diagonal blocks are fully observed, and off-diagonal blocks are randomly sampled with sampling rate $s = 15\%$, yielding an overall sampling rate of 25.625%.

5.4.1 Random disks

We present a visual comparison of reconstructions over different samples in Figure 7 with clean data, and Figure 8 with 5% noise. A summary of errors over the testing dataset in both cases is shown in Table 1. In the noiseless setting, the full-data solver with full measurements achieves the best accuracy across all metrics, representing the solver’s best attainable performance. Using the same solver with diffusion-completed measurements from sparse data yields the closest performance to the best possible reconstructions. The direct sparse-data solver lags behind across all metrics, consistent with the observed blur and boundary erosion. Although H-matrix completion outperforms the direct sparse-data solver and is slightly worse than diffusion completion, it requires a much higher sampling rate (25.625%) compared to the other cases (1%). With 5% noise, all methods degrade slightly; diffusion completion remains superior to both the direct sparse-data solver and H-matrix completion.

Table 1: Reconstruction results for the **Disks** dataset. **First row:** best possible reconstruction using full data. **Last three rows:** various inverse problem solving strategies with sparse data. The overall sampling rate is indicated in the brackets, and the best results with sparse data are marked in bold.

Method	Noiseless DtN			5% Noisy DtN		
	SSIM↑	RE↓	MAE↓	SSIM↑	RE↓	MAE↓
full-data solver (100%)	0.819	20.7%	0.176	0.808	21.6%	0.186
diffusion completion (1%) + full-data solver	0.774	33.4%	0.288	0.762	34.4%	0.302
direct sparse-data solver (1%)	0.597	44.9%	0.495	0.578	46.5%	0.524
H-matrix completion (25.625%) + full-data solver	0.730	41.4%	0.361	0.712	43.7%	0.388

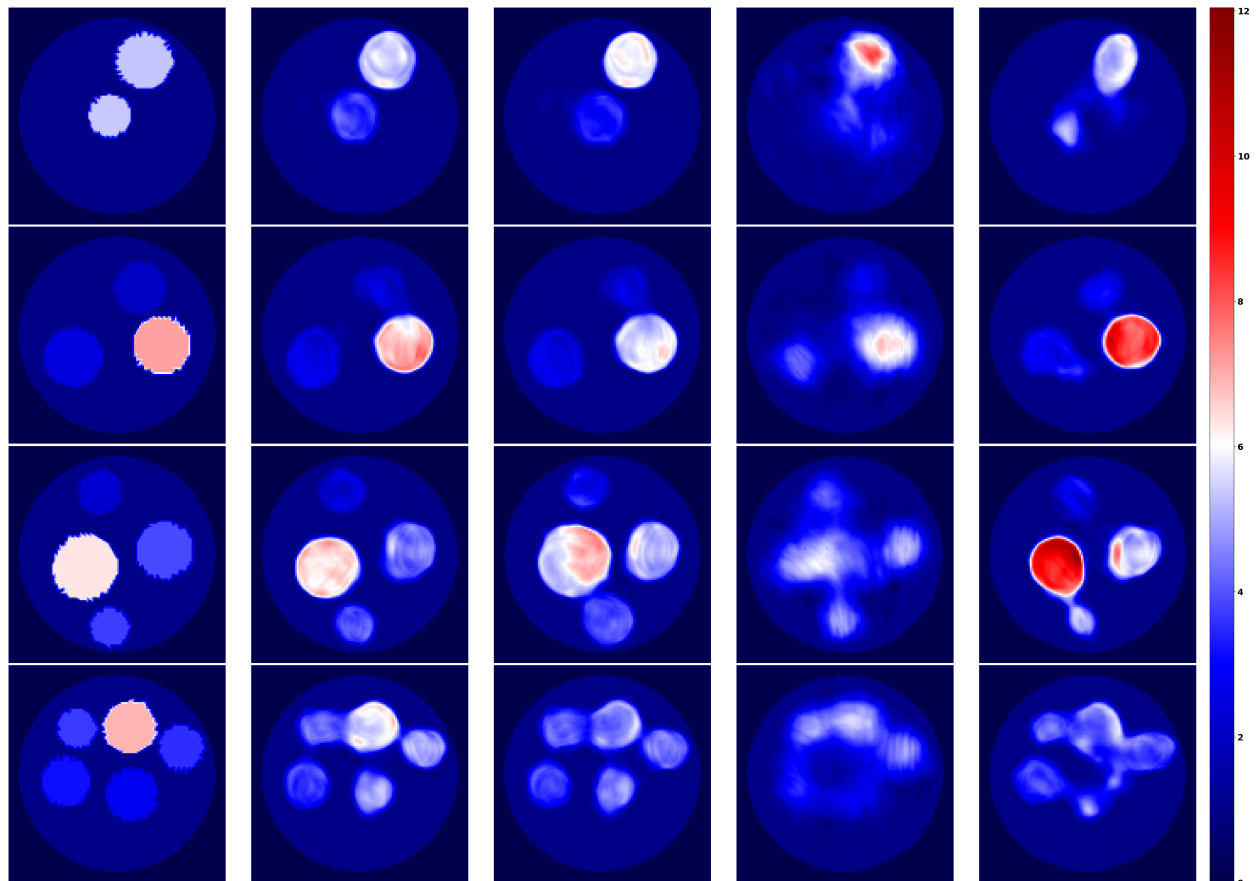


Figure 7: Reconstructions from the *noiseless random disks* dataset. **Columns (left→right):** (1) *Ground truth* conductivity; (2) *Best possible reconstruction* from the full-data solver (overall sampling rate 100%); (3) Reconstructions from the full-data solver applied to *diffusion completion* of measurements (overall sampling rate 1%); (4) Reconstructions from the *direct sparse-data solver* (overall sampling rate 1%); (5) Reconstructions from the full-data solver applied to *H-matrix completion* of measurements (overall sampling rate 25.625%). **Rows (top→bottom):** Examples with number of disks $n = 2, 3, 4, 5$.

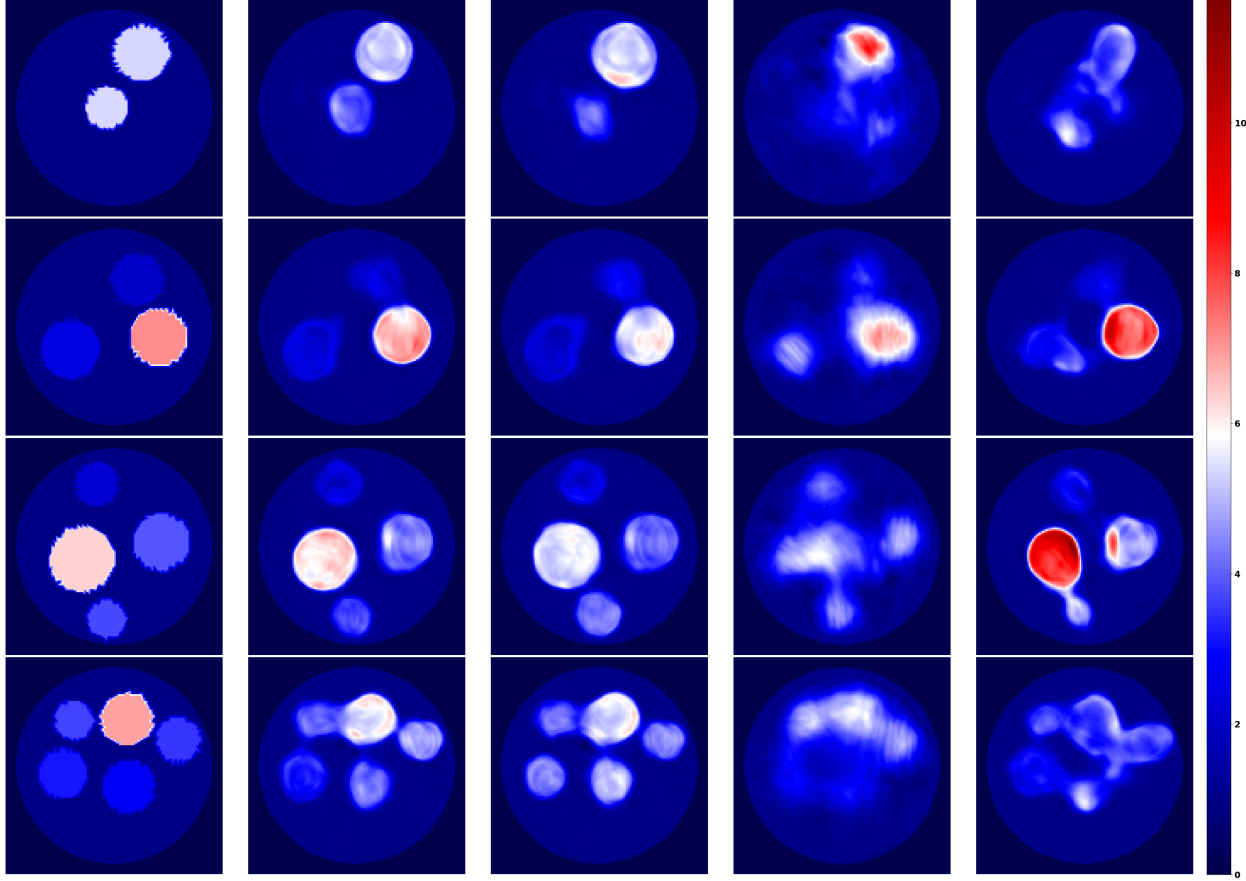


Figure 8: Reconstructions from the **random disks** dataset with 5% noise. **Columns (left→right):** (1) *Ground truth* conductivity; (2) *Best possible reconstruction* from the full-data solver (overall sampling rate 100%); (3) Reconstructions from the full-data solver applied to *diffusion completion* of measurements (overall sampling rate 1%); (4) Reconstructions from the *direct sparse-data solver* (overall sampling rate 1%); (5) Reconstructions from the full-data solver applied to *H-matrix completion* of measurements (overall sampling rate 25.625%). **Rows (top→bottom):** Examples with number of disks $n = 2, 3, 4, 5$.

5.4.2 Random Shepp-Logan phantoms

The same experiments and comparisons are conducted for the Shepp–Logan dataset with visual reconstructions in Figs. 9 and 10, and errors shown in Table 2. In the noiseless setting, diffusion completion + full-data solver produces reconstructions close to the best possible result, preserving the thin skull boundary and the intracranial cavities. Unlike the Disks dataset, the direct sparse-data solver performs better than H-matrix completion on Shepp–Logan: the direct sparse-data solver recovers the main structures but tends to smooth thin features, whereas H-matrix completion + full-data solver fails to recover both the skull boundary and the cavities. With 5% noise, robustness differences become more apparent. The best possible reconstruction and the diffusion-completion strategy both remain stable, while the direct sparse-data solver exhibits edge distortions at the boundary and amplified blur artifacts in the zoomed region. The H-matrix completion + full-data solver continues to fail as in the noiseless setting. Overall, diffusion completion narrows the gap to the best possible reconstruction across all metrics and maintains this advantage under noise, whereas the direct sparse-data solver and H-matrix completion struggle to solve the inverse problem.

6 Conclusion and Discussion

We have proposed a diffusion-based DtN completion framework for EIT with extremely sparse boundary measurements and evaluated it on the Disks and Shepp–Logan datasets. Using the same inverse solver across all settings, reconstructions from diffusion completion are consistently closest to the best possible reconstruction that uses full measurements among the direct sparse-data solver and H-matrix completion. These results support our diffusion completion design

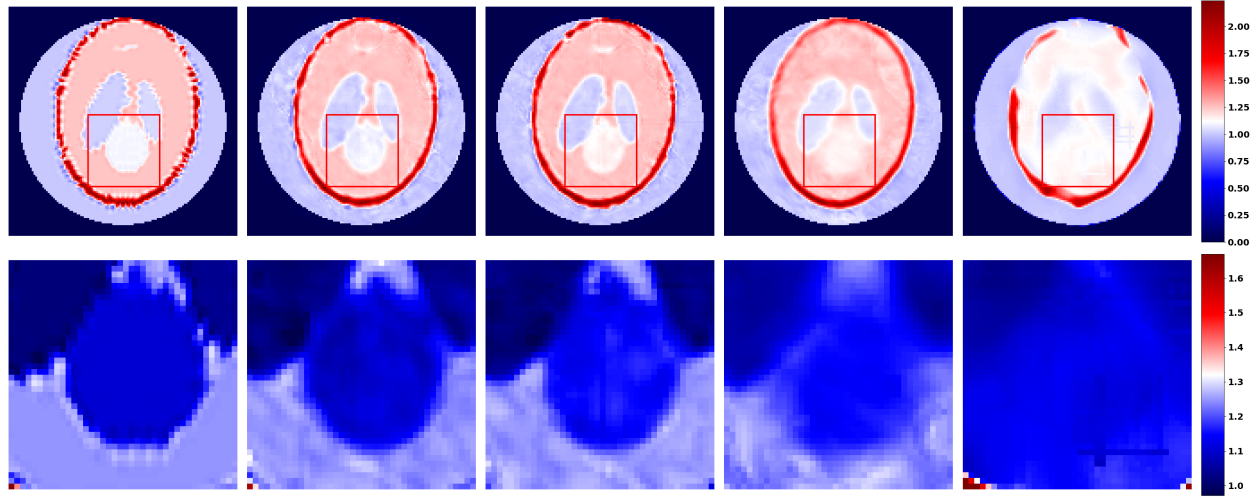


Figure 9: Reconstructions from the **noiseless Shepp-Logan** dataset. **Columns (left→right):** (1) *Ground truth* conductivity; (2) *Best possible reconstruction* from the full-data solver (overall sampling rate 100%); (3) Reconstructions from the full-data solver applied to *diffusion completion* of measurements (overall sampling rate 1%); (4) Reconstructions from the *direct sparse-data solver* (overall sampling rate 1%); (5) Reconstructions from the full-data solver applied to *H-matrix completion* of measurements (overall sampling rate 25.625%). **Rows (top→bottom):** full field of view (top) with a red box indicating the zoom region; zoomed-in crops of that region (bottom).

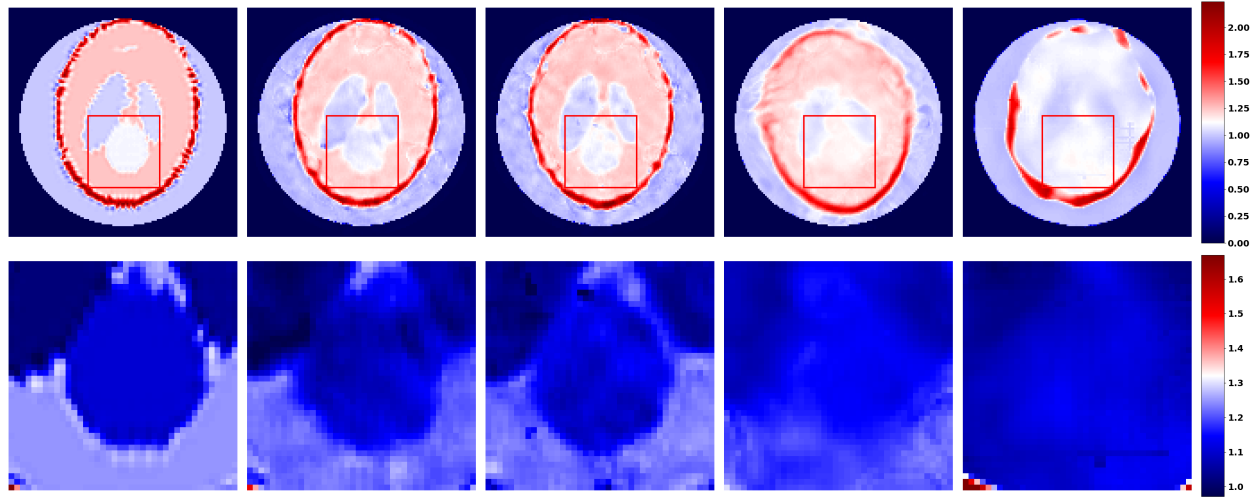


Figure 10: Reconstructions from the random **Shepp-Logan** dataset 5% noise. **Columns (left→right):** (1) *Ground truth* conductivity; (2) *Best possible reconstruction* from the full-data solver (overall sampling rate 100%); (3) Reconstructions from the full-data solver applied to *diffusion completion* of measurements (overall sampling rate 1%); (4) Reconstructions from the *direct sparse-data solver* (overall sampling rate 1%); (5) Reconstructions from the full-data solver applied to *H-matrix completion* of measurements (overall sampling rate 25.625%). **Rows (top→bottom):** full field of view (top) with a red box indicating the zoom region; zoomed-in crops of that region (bottom).

Table 2: Reconstruction results for the **Shepp–Logan** dataset. **First row:** best possible reconstruction using full data. **Last three rows:** various inverse problem solving strategies with sparse data. The overall sampling rate is indicated in the brackets, and the best results with sparse data are marked in bold.

Method	Noiseless DtN			5% Noisy DtN		
	SSIM↑	RE↓	MAE↓	SSIM↑	RE↓	MAE↓
full-data solver (100%)	0.930	8.2%	0.030	0.898	10.2%	0.042
diffusion completion (1%) + full-data solver	0.910	10.3%	0.036	0.842	14.3%	0.055
direct sparse-data solver (1%)	0.886	11.3%	0.043	0.776	16.4%	0.075
H-matrix completion (25.625%) + full-data solver	0.825	17.0%	0.067	0.788	19.5%	0.085

that improves stability and accuracy without modifying the inverse solvers on-the-shelf. Our analysis shows that the discretized DtN measurement set $F_N(K)$ inherits the low-dimensional structure of the polygon conductivity class K . The intrinsic complexity of DtN measurements can be controlled via a metric entropy bound determined by the underlying parameter dimension $2n_v$, rather than by the ambient measurement dimension. Combining this complexity estimate with the conditional diffusion-model convergence theorem yields a nonasymptotic end-to-end completion guarantee in our EIT setting, with an explicit dependence on the diffusion steps T and vertices n_v .

We next outline several promising directions for further development. First, although we considered simulated data in this paper, diffusion completion can be directly applied to real EIT application provided sufficient lab data are available for training. Second, encoding structure of the DtN matrix can improve generalization and data efficiency. In addition to hierarchical low-rankness [Bebendorf and Hackbusch, 2003, Ballani and Kressner, 2017], DtN measurements in our setting are symmetric and satisfy zero row or column sum constraints [Somersalo et al., 1992], which can be enforced by specific network architectural designs or training penalties. Third, accelerating sampling is important for practical deployment. Distillation [Song et al., 2023] and few-step samplers [Song et al., 2020a] in diffusion models can be directly incorporated into our framework and reduce inference cost while maintaining accuracy on conditional tasks. Fourth, the generative measurement prior can guide the choice of boundary signals. Expected information gain provides a clear objective for selecting informative measurements, and modern Bayesian optimal experimental design methods make this feasible in EIT settings [Dong et al., 2025, Hellmuth et al., 2025].

7 Acknowledgements

The authors were partially supported by the US National Science Foundation under awards DMS-2244988, CAIG RISE-2530596, IIS-2520978, and the DARPA D24AP00325-00.

References

Giovanni S Alberti, Ángel Arroyo, and Matteo Santacesaria. Inverse problems on low-dimensional manifolds. *Nonlinearity*, 36(1):734, 2022.

Giovanni S Alberti, Johannes Hertrich, Matteo Santacesaria, and Silvia Sciuotto. Manifold learning by mixture models of vaes for inverse problems. *Journal of Machine Learning Research*, 25(202):1–35, 2024.

Giovanni Alessandrini. Stable determination of conductivity by boundary measurements. *Applicable Analysis*, 27(1-3): 153–172, 1988.

Alen Alexanderian. Optimal experimental design for infinite-dimensional bayesian inverse problems governed by pdes: A review. *Inverse Problems*, 37(4):043001, 2021.

Andrew Allers and Fadil Santosa. Stability and resolution analysis of a linearized problem in electrical impedance tomography. *Inverse problems*, 7(4):515, 1991.

Melody Alsaker, Sarah Jane Hamilton, and Andreas Hauptmann. A direct d-bar method for partial boundary data electrical impedance tomography with a priori information. *Inverse Problems and Imaging*, 11(3):427–454, 2017.

Brian DO Anderson. Reverse-time diffusion equation models. *Stochastic Processes and their Applications*, 12(3): 313–326, 1982.

Simon R Arridge. Optical tomography in medical imaging. *Inverse problems*, 15(2):R41, 1999.

Kari Astala and Lassi Päiväranta. Calderón’s inverse conductivity problem in the plane. *Annals of Mathematics*, pages 265–299, 2006.

Iskander Azangulov, George Deligiannidis, and Judith Rousseau. Convergence of diffusion models under the manifold hypothesis in high-dimensions. *arXiv preprint arXiv:2409.18804*, 2024.

Guillaume Bal. Introduction to inverse problems. *Lecture Notes-Department of Applied Physics and Applied Mathematics, Columbia University, New York*, 2012.

Jonas Ballani and Daniel Kressner. Matrices with hierarchical low-rank structures. In *Exploiting Hidden Structure in Matrix Computations: Algorithms and Applications: Cetraro, Italy 2015*, pages 161–209. Springer, 2017.

Georgios Batzolis, Jan Stanczuk, Carola-Bibiane Schönlieb, and Christian Etmann. Conditional image generation with score-based diffusion models. *arXiv preprint arXiv:2111.13606*, 2021.

Mario Bebendorf and Wolfgang Hackbusch. Existence of h-matrix approximants to the inverse fe-matrix of elliptic operators with l^∞ -coefficients. *Numerische Mathematik*, 95(1):1–28, 2003.

Sebastian Bechtel and El Maati Ouhabaz. Off-diagonal bounds for the dirichlet-to-neumann operator on lipschitz domains. *Journal of Mathematical Analysis and Applications*, 530(2):127696, 2024.

Joe Benton, Valentin De Bortoli, Arnaud Doucet, and George Deligiannidis. Nearly d -linear convergence bounds for diffusion models via stochastic localization. *arXiv preprint arXiv:2308.03686*, 2023.

Elena Beretta and Elisa Francini. Global lipschitz stability estimates for polygonal conductivity inclusions from boundary measurements. *Applicable Analysis*, 101(10):3536–3549, 2022.

Elena Beretta, Elisa Francini, and Sergio Vessella. Differentiability of the dirichlet to neumann map under movements of polygonal inclusions with an application to shape optimization. *SIAM Journal on Mathematical Analysis*, 49(2): 756–776, 2017.

Amit Bhat, Ke Chen, and Chunmei Wang. Neural correction operator: A reliable and fast approach for electrical impedance tomography. *arXiv preprint arXiv:2507.18875*, 2025.

Marc Bonnet and Andrei Constantinescu. Inverse problems in elasticity. *Inverse problems*, 21(2):R1, 2005.

Liliana Borcea. Electrical impedance tomography. *Inverse problems*, 18(6):R99, 2002.

Liliana Borcea, Fernando Guevara Vasquez, and Alexander V Mamonov. Study of noise effects in electrical impedance tomography withresistor networks. *Inverse Problems and Imaging*, 7(2):417–443, 2013.

Tan Bui-Thanh, Qin Li, and Leonardo Zepeda-Núñez. Bridging and improving theoretical and computational electrical impedance tomography via data completion. *SIAM Journal on Scientific Computing*, 44(3):B668–B693, 2022.

Fabien Caubet, Marc Dambrine, and Helmut Harbrecht. A new method for the data completion problem and application to obstacle detection. *SIAM Journal on Applied Mathematics*, 79(1):415–435, 2019.

Siyu Cen, Bangti Jin, Kwancheol Shin, and Zhi Zhou. Electrical impedance tomography with deep calderón method. *Journal of Computational Physics*, 493:112427, 2023.

Hongrui Chen, Holden Lee, and Jianfeng Lu. Improved analysis of score-based generative modeling: User-friendly bounds under minimal smoothness assumptions. In *International Conference on Machine Learning*, pages 4735–4763. PMLR, 2023.

Ke Chen, Jasen Lai, and Chunmei Wang. Pseudo-differential integral autoencoder network for inverse pde operators. *Inverse Problems*, 40(10):105004, 2024.

Margaret Cheney, David Isaacson, Jonathan C Newell, S Simske, and J Goble. Noser: An algorithm for solving the inverse conductivity problem. *International Journal of Imaging systems and technology*, 2(2):66–75, 1990.

Yat Tin Chow, Kazufumi Ito, and Jun Zou. A direct sampling method for electrical impedance tomography. *Inverse Problems*, 30(9):095003, 2014.

Yat Tin Chow, Fuqun Han, and Jun Zou. A direct sampling method for simultaneously recovering inhomogeneous inclusions of different nature. *SIAM Journal on Scientific Computing*, 43(3):A2161–A2189, 2021.

M. Chung. Randomized shepp-logan phantom. <https://github.com/matthiaschung/Random-Shepp-Logan-Phantom>, 2020.

D Colton and PB Monk. Target identification of coated objects. *IEEE transactions on antennas and propagation*, 54(4):1232–1242, 2006.

Jiayuan Dong, Christian Jacobsen, Mehdi Khalloufi, Maryam Akram, Wanjiao Liu, Karthik Duraisamy, and Xun Huan. Variational bayesian optimal experimental design with normalizing flows. *Computer Methods in Applied Mechanics and Engineering*, 433:117457, 2025.

Fangfang Dou, Xiaodong Liu, Shixu Meng, and Bo Zhang. Data completion algorithms and their applications in inverse acoustic scattering with limited-aperture backscattering data. *Journal of Computational Physics*, 469:111550, 2022.

Lawrence C Evans. *Partial differential equations*, volume 19. American mathematical society, 2022.

Javier García-Martín, Jaime Gómez-Gil, and Ernesto Vázquez-Sánchez. Non-destructive techniques based on eddy current testing. *Sensors*, 11(3):2525–2565, 2011.

Jinwoo Go and Peng Chen. Accurate, scalable, and efficient bayesian optimal experimental design with derivative-informed neural operators. *Computer Methods in Applied Mechanics and Engineering*, 438:117845, 2025.

Ruchi Guo, Shuhao Cao, and Long Chen. Transformer meets boundary value inverse problem. In *International Conference on Learning Representations*. ICLR, 2023.

Eldad Haber, Uri M Ascher, and Doug Oldenburg. On optimization techniques for solving nonlinear inverseproblems. *Inverse problems*, 16(5):1263, 2000.

Sarah Jane Hamilton and Andreas Hauptmann. Deep d-bar: Real-time electrical impedance tomography imaging with deep neural networks. *IEEE transactions on medical imaging*, 37(10):2367–2377, 2018.

Martin Hanke. Regularizing properties of a truncated newton-cg algorithm for nonlinear inverse problems. *Numerical Functional Analysis and Optimization*, 18(9-10):971–993, 1997.

Bastian Harrach. Interpolation of missing electrode data in electrical impedance tomography. *Inverse Problems*, 31(11):115008, 2015.

Andreas Hauptmann. Approximation of full-boundary data from partial-boundary electrode measurements. *Inverse Problems*, 33(12):125017, 2017.

Serge JH Heines, Tobias H Becher, Iwan CC van der Horst, and Dennis CJJ Bergmans. Clinical applicability of electrical impedance tomography in patient-tailored ventilation: a narrative review. *Tomography*, 9(5):1903–1932, 2023.

Kathrin Hellmuth, Ruhui Jin, Qin Li, and Stephen J Wright. Data selection: at the interface of pde-based inverse problem and randomized linear algebra. *arXiv preprint arXiv:2510.01567*, 2025.

Jonathan Ho, Ajay Jain, and Pieter Abbeel. Denoising diffusion probabilistic models. *Advances in neural information processing systems*, 33:6840–6851, 2020.

Xun Huan and Youssef M Marzouk. Simulation-based optimal bayesian experimental design for nonlinear systems. *Journal of Computational Physics*, 232(1):288–317, 2013.

Aapo Hyvärinen and Peter Dayan. Estimation of non-normalized statistical models by score matching. *Journal of Machine Learning Research*, 6(4), 2005.

Nuutti Hyvönen, Altti Jääskeläinen, Ruma Maity, and Anton Vavilov. Bayesian experimental design for head imaging by electrical impedance tomography. *SIAM Journal on Applied Mathematics*, 84(4):1718–1741, 2024.

Victor Isakov. *Inverse problems for partial differential equations*. Springer, 2006.

Hanyang Jiang, Yuehaw Khoo, and Haizhao Yang. Reinforced inverse scattering. *SIAM Journal on Scientific Computing*, 46(6):B884–B902, 2024.

Bangti Jin, Taufiquar Khan, and Peter Maass. A reconstruction algorithm for electrical impedance tomography based on sparsity regularization. *International Journal for Numerical Methods in Engineering*, 89(3):337–353, 2012.

Ruhui Jin, Qin Li, Stephen O Mussmann, and Stephen J Wright. Continuous nonlinear adaptive experimental design with gradient flow. *arXiv preprint arXiv:2411.14332*, 2024.

Tero Karras, Miika Aittala, Timo Aila, and Samuli Laine. Elucidating the design space of diffusion-based generative models. *Advances in neural information processing systems*, 35:26565–26577, 2022.

Karina Koval and Ruanui Nicholson. Non-intrusive optimal experimental design for large-scale nonlinear bayesian inverse problems using a bayesian approximation error approach: K. koval, r. nicholson. *Journal of Scientific Computing*, 104(3):98, 2025.

Jingzhi Li, Peijun Li, Hongyu Liu, and Xiaodong Liu. Recovering multiscale buried anomalies in a two-layered medium. *Inverse Problems*, 31(10):105006, 2015.

Jiadong Liang, Zhihan Huang, and Yuxin Chen. Low-dimensional adaptation of diffusion models: Convergence in total variation. *arXiv preprint arXiv:2501.12982*, 2025.

Ilya Loshchilov and Frank Hutter. Decoupled weight decay regularization. *arXiv preprint arXiv:1711.05101*, 2017.

Roberto Molinaro, Yunan Yang, Björn Engquist, and Siddhartha Mishra. Neural inverse operators for solving pde inverse problems. In *International Conference on Machine Learning*, pages 25105–25139. PMLR, 2023.

Jennifer L Mueller and Samuli Siltanen. The d-bar method for electrical impedance tomography—demystified. *Inverse problems*, 36(9):093001, 2020.

Adrian I Nachman. Global uniqueness for a two-dimensional inverse boundary value problem. *Annals of Mathematics*, pages 71–96, 1996.

Yong Zheng Ong, Zuowei Shen, and Haizhao Yang. Integral autoencoder network for discretization-invariant learning. *Journal of Machine Learning Research*, 23(286):1–45, 2022.

R Gerhard Pratt. Seismic waveform inversion in the frequency domain, part 1: Theory and verification in a physical scale model. *Geophysics*, 64(3):888–901, 1999.

Christian Putensen, Benjamin Hentze, Stefan Muenster, and Thomas Muders. Electrical impedance tomography for cardio-pulmonary monitoring. *Journal of clinical medicine*, 8(8):1176, 2019.

Benjamin Recht. A simpler approach to matrix completion. *Journal of Machine Learning Research*, 12(12), 2011.

Olaf Ronneberger, Philipp Fischer, and Thomas Brox. U-net: Convolutional networks for biomedical image segmentation. In *International Conference on Medical image computing and computer-assisted intervention*, pages 234–241. Springer, 2015.

Gaetano Scaramuzzo, Bertrand Pavlovsky, Andy Adler, Walter Baccinelli, Dani L Bodor, L Felipe Damiani, Guillaume Franchineau, Juliette Francovich, Inéz Frerichs, Juan A Sánchez Giralt, et al. Electrical impedance tomography monitoring in adult icu patients: state-of-the-art, recommendations for standardized acquisition, processing, and clinical use, and future directions. *Critical Care*, 28(1):377, 2024.

Ziju Shen, Yufei Wang, Dufan Wu, Xu Yang, and Bin Dong. Learning to scan: A deep reinforcement learning approach for personalized scanning in ct imaging. *Inverse Problems & Imaging*, 16(1), 2022.

Lawrence A Shepp and Benjamin F Logan. The fourier reconstruction of a head section. *IEEE Transactions on nuclear science*, 21(3):21–43, 1974.

Erkki Somersalo, Margaret Cheney, and David Isaacson. Existence and uniqueness for electrode models for electric current computed tomography. *SIAM Journal on Applied Mathematics*, 52(4):1023–1040, 1992.

Jiaming Song, Chenlin Meng, and Stefano Ermon. Denoising diffusion implicit models. *arXiv preprint arXiv:2010.02502*, 2020a.

Yang Song, Jascha Sohl-Dickstein, Diederik P Kingma, Abhishek Kumar, Stefano Ermon, and Ben Poole. Score-based generative modeling through stochastic differential equations. *arXiv preprint arXiv:2011.13456*, 2020b.

Yang Song, Prafulla Dhariwal, Mark Chen, and Ilya Sutskever. Consistency models. In *Proceedings of the 40th International Conference on Machine Learning*, pages 32211–32252, 2023.

John Sylvester and Gunther Uhlmann. A global uniqueness theorem for an inverse boundary value problem. *Annals of mathematics*, pages 153–169, 1987.

Rong Tang, Lizhen Lin, and Yun Yang. Conditional diffusion models are minimax-optimal and manifold-adaptive for conditional distribution estimation. *arXiv preprint arXiv:2409.20124*, 2024.

Albert Tarantola and Bernard Valette. Generalized nonlinear inverse problems solved using the least squares criterion. *Reviews of Geophysics*, 20(2):219–232, 1982.

Gunther Uhlmann. Electrical impedance tomography and calderón’s problem. *Inverse problems*, 25(12):123011, 2009.

Gunther Uhlmann. *Inverse problems and applications: Inside out II*, volume 60. Cambridge University Press, 2013.

Stefan Van der Walt, Johannes L Schönberger, Juan Nunez-Iglesias, François Boulogne, Joshua D Warner, Neil Yager, Emmanuelle Gouillart, and Tony Yu. scikit-image: image processing in python. *PeerJ*, 2:e453, 2014.

Marko Vauhkonen, Dénes Vadász, Pasi A Karjalainen, Erkki Somersalo, and Jari P Kaipio. Tikhonov regularization and prior information in electrical impedance tomography. *IEEE transactions on medical imaging*, 17(2):285–293, 2002.

Pascal Vincent. A connection between score matching and denoising autoencoders. *Neural computation*, 23(7):1661–1674, 2011.

A Uniform Lipschitz boundary for convex admissible polygons

Definition A.1 (Lipschitz boundary class). *Fix constants $r_0 > 0$ and $K_0 > 1$. We say that an open set $D \subset \mathbb{R}^2$ has Lipschitz boundary of class (r_0, K_0) if for every point $x_0 \in \partial D$ there exist a rigid motion \mathcal{T}_{x_0} (a translation followed by a rotation) with $\mathcal{T}_{x_0}(x_0) = 0$ and a K_0 -Lipschitz function $\phi : [-r_0, r_0] \rightarrow \mathbb{R}$ such that*

$$\mathcal{T}_{x_0}(D) \cap ([-r_0, r_0] \times [-K_0 r_0, K_0 r_0]) = \{(x_1, x_2) : x_1 \in [-r_0, r_0], x_2 > \phi(x_1)\}.$$

Lemma A.1 (Uniform Lipschitz boundary for convex admissible polygons). *Let $P = P(v) \in \mathcal{A}$, ∂P is of Lipschitz class (r_0, K_0) with the uniform choices*

$$r_0 := \frac{d_1}{4}, \quad K_0 := \cot\left(\frac{\beta_0}{2}\right).$$

Proof. Fix $x_0 \in \partial P$. We distinguish two cases.

Case 1: x_0 lies in the relative interior of an edge. Let $e = [v_i, v_{i+1}]$ be that edge. Since $|v_{i+1} - v_i| \geq d_1$, the ball $B_2(x_0, r_0)$ with $r_0 = d_1/4$ intersects ∂P only along the segment of e (no vertex is contained in the ball). After a rigid motion sending x_0 to 0 and rotating so that e becomes $\{x_2 = 0\}$, the convexity implies that in a small neighborhood P coincides with either $\{x_2 > 0\}$ or $\{x_2 < 0\}$, hence the Lipschitz representation holds with Lipschitz constant 0.

Case 2: x_0 is a vertex, say $x_0 = v_i$. Translate v_i to 0. Let the two incident edges be the rays along the lines ℓ_- and ℓ_+ meeting at interior angle $\beta_i \in [\beta_0, \pi]$. Rotate coordinates so that the bisector of the interior angle is the x_2 -axis. Then each line ℓ_{\pm} makes an angle $\beta_i/2$ with the x_2 -axis, hence an angle $\pi/2 - \beta_i/2$ with the x_1 -axis. Therefore each ℓ_{\pm} is the graph of an affine function $x_2 = \phi_{\pm}(x_1)$ with slope bounded by

$$|\phi'_{\pm}(x_1)| = \tan\left(\frac{\pi}{2} - \frac{\beta_i}{2}\right) = \cot\left(\frac{\beta_i}{2}\right) \leq \cot\left(\frac{\beta_0}{2}\right) = K_0.$$

Since $|v_{i\pm 1} - v_i| \geq d_1$, the ball $B_2(0, r_0)$ with $r_0 = d_1/4$ intersects ∂P only along these two edges. In the above coordinates, $P \cap B_2(0, r_0)$ coincides with the epigraph $\{x_2 > \phi(x_1)\}$ where $\phi := \max\{\phi_-, \phi_+\}$, and ϕ is K_0 -Lipschitz.

Combining the two cases gives that ∂P is of Lipschitz class (r_0, K_0) with the stated uniform constants. \square

B Proof for Lemma 4.2

We first show a useful fact that perturbing vertices by δ leads to at most δ perturbation around the polygonal boundary in Hausdorff distance.

Lemma B.1 (Boundary perturbation under vertex perturbations). *Let $v, w \in \mathcal{V}^{n_v}$ be counterclockwise ordered vertex, then*

$$d_H(\partial P(v), \partial P(w)) \leq \|v - w\|_{\text{poly}}.$$

Moreover, if $P(v) \subset \Omega$ and $P(w) \subset \Omega$, then $\text{dist}(P(u), \partial \Omega) = \text{dist}(\partial P(u), \partial \Omega)$ for $u = v, w$, and

$$\text{dist}(P(v), \partial \Omega) \geq \text{dist}(P(w), \partial \Omega) - \|v - w\|_{\text{poly}}.$$

Proof. Fix i and consider the segments $e_i(v) = [v_i, v_{i+1}]$ and $e_i(w) = [w_i, w_{i+1}]$. For any $t \in [0, 1]$, set $x(t) = (1-t)v_i + tw_{i+1} \in e_i(v)$ and $y(t) = (1-t)w_i + tv_{i+1} \in e_i(w)$. Then

$$|x(t) - y(t)| \leq (1-t)|v_i - w_i| + t|v_{i+1} - w_{i+1}| \leq \|v - w\|_{\text{poly}}.$$

Consequently, we have

$$\text{dist}(x(t), e_i(w)) \leq \|v - w\|_{\text{poly}}.$$

Taking the supremum over $t \in [0, 1]$ yields

$$\sup_{x \in e_i(v)} \text{dist}(x, e_i(w)) \leq \|v - w\|_{\text{poly}}. \quad (23)$$

Consider $x \in \partial P(v)$, then $x \in e_i(v)$ for some i , and since $e_i(w) \subset \partial P(w)$ we have

$$\text{dist}(x, \partial P(w)) \leq \text{dist}(x, e_i(w)) \leq \|v - w\|_{\text{poly}},$$

where the last inequality results from Equation 23. Taking the supremum over $x \in \partial P(v)$ gives $\sup_{x \in \partial P(v)} \text{dist}(x, \partial P(w)) \leq \|v - w\|_{\text{poly}}$. Since $\partial P(v)$ and $\partial P(w)$ are unions of the corresponding edges,

we also obtain $\sup_{x \in \partial P(v)} \text{dist}(x, \partial P(w)) \leq \|v - w\|_{\text{poly}}$. By symmetry (exchanging v and w) we also have $\sup_{y \in \partial P(w)} \text{dist}(y, \partial P(v)) \leq \|v - w\|_{\text{poly}}$, proving the Hausdorff estimate.

For $P(v) \subset \Omega$, since $P(v)$ is compact and $\partial\Omega$ is closed, any point $x \in P(v)$ minimizing $\text{dist}(x, \partial\Omega)$ must lie on $\partial P(v)$: if x were in the interior of $P(v)$, one could move slightly toward a nearest boundary point of $\partial\Omega$ while staying inside $P(v)$ and decrease the distance, a contradiction. Hence $\text{dist}(P(v), \partial\Omega) = \text{dist}(\partial P(v), \partial\Omega)$.

For the distance inequality, note that if $d_H(A, A') \leq \delta$ for nonempty closed sets, then $\text{dist}(A, B) \geq \text{dist}(A', B) - \delta$ for any closed B , by the triangle inequality in \mathbb{R}^2 . \square

Now we can prove Lemma 4.2 as follows.

Proof of Lemma 4.2. Write $e_i^* := [v_i^*, v_{i+1}^*]$ for the edges of ∂P^* . Since P^* is convex, ∂P^* is simple, and every pair of nonadjacent edges is disjoint. Hence

$$\eta^* := \frac{1}{2} \min \{ \text{dist}(e_i^*, e_j^*) : e_i^*, e_j^* \text{ nonadjacent} \} > 0.$$

Moreover, since $P^* \in \mathcal{A}_{1/2}$, we have the strict margins

$$m_0 := \text{dist}(P^*, \partial\Omega) - \frac{1}{2}d_0 > 0, \quad m_1 := \min_i |v_{i+1}^* - v_i^*| - \frac{1}{2}d_1 > 0, \quad \beta_s := \min_i \{ \beta_i(v^*) - \frac{1}{2}\beta_0, \pi - \frac{1}{2}\beta_0 - \beta_i(v^*) \} > 0.$$

For any i ,

$$| |v_{i+1} - v_i| - |v_{i+1}^* - v_i^*| | \leq |(v_{i+1} - v_{i+1}^*) - (v_i - v_i^*)| \leq 2\|v - v^*\|_{\text{poly}}.$$

Thus if $\|v - v^*\|_{\text{poly}} < m_1/4$, then $|v_{i+1} - v_i| > d_1/2$ for all i , i.e. (A2') holds.

For each edge $e_i(v) = [v_i, v_{i+1}]$, the same interpolation argument as in Lemma B.1 gives $d_H(e_i(v), e_i^*) \leq \|v - v^*\|_{\text{poly}}$. Hence for any nonadjacent edge index pair (i, j) ,

$$\text{dist}(e_i(v), e_j(v)) \geq \text{dist}(e_i^*, e_j^*) - d_H(e_i(v), e_i^*) - d_H(e_j(v), e_j^*) \geq 2\eta^* - 2\|v - v^*\|_{\text{poly}}.$$

If $\|v - v^*\|_{\text{poly}} < \eta^*$, then $\text{dist}(e_i(v), e_j(v)) > 0$ for all nonadjacent pairs, so nonadjacent edges cannot intersect. Moreover, once we also enforce the angle lower bound $\beta_i(v) > \beta_0/2$ for all i (proved below), adjacent edges cannot overlap. Hence $\partial P(v)$ is a simple closed polygonal curve.

Now we show the inclusion in Ω and the boundary margin. Since $P^* \subset \Omega$ and $\text{dist}(P^*, \partial\Omega) > d_0/2$, every vertex satisfies $\text{dist}(v_i^*, \partial\Omega) \geq \text{dist}(P^*, \partial\Omega) > 0$. Set

$$\eta_\Omega^* := \frac{1}{2} \text{dist}(P^*, \partial\Omega) > 0.$$

If $\|v - v^*\|_{\text{poly}} < \eta_\Omega^*$, then $|v_i - v_i^*| < \eta_\Omega^*$ for all i , hence $v_i \in \Omega$ for all i . As Ω is convex, each edge $[v_i, v_{i+1}] \subset \Omega$ and therefore $P(v) \subset \Omega$. Furthermore, by Lemma B.1,

$$\text{dist}(P(v), \partial\Omega) \geq \text{dist}(P^*, \partial\Omega) - \|v - v^*\|_{\text{poly}}.$$

Thus if $\|v - v^*\|_{\text{poly}} < m_0$, then $\text{dist}(P(v), \partial\Omega) > d_0/2$, i.e. (A1') holds.

We now consider the angle bounds and convexity in (A3'). On the set where (A2') holds, the interior angles $\beta_i(v)$ are continuous functions of v (e.g. they can be expressed via dot/cross products of the adjacent edge vectors). Hence there exists $\rho_{\text{ang}} > 0$ such that if $\|v - v^*\|_{\text{poly}} < \rho_{\text{ang}}$ then $|\beta_i(v) - \beta_i(v^*)| < \beta_s/2$ for all i , and consequently $\beta_0/2 < \beta_i(v) < \pi - \beta_0/2$ for all i , which yields (A3').

Finally, define

$$\rho_{P^*} := \min \{ \eta^*, \eta_\Omega^*, m_0, m_1/4, \rho_{\text{ang}} \}.$$

Then $\|v - v^*\|_{\text{poly}} < \rho_{P^*}$ implies (A1')–(A3'). \square

C Proof of Lemma 4.3

Lemma C.1. *There exists a constant $C_H > 0$, depending only on the a priori data, such that for all $P, Q \in \mathcal{A}_{1/2}$,*

$$d_H(\partial P, \partial Q) \leq C_H \|\gamma_P - \gamma_Q\|_{L^1(\Omega)}^{1/2}.$$

Proof of Lemma C.1. Let $\delta := d_H(\partial P, \partial Q)$. It suffices to prove the case when $\delta > 0$. Without loss of generality, we can choose $x \in \partial P$ such that $\text{dist}(x, \partial Q) = \delta$ since ∂P is compact. Consider open ball $\tilde{B}_2(x, \delta)$, $\tilde{B}_2(x, \delta) \cap \partial Q = \emptyset$, hence χ_Q is constant on $\tilde{B}_2(x, \delta)$.

Since ∂P is Lipschitz of class (r_0, K_0) , at x there exist local coordinates in which P coincides with $\{(x_1, x_2) : x_2 > \phi(x_1)\}$, with ϕ K_0 -Lipschitz. In these coordinates, for any $h \leq \min\{r_0, \delta/2\}$ the truncated cone

$$C^+(h) := \{(x_1, x_2) : 0 < x_2 < h, |x_1| < x_2/K_0\}$$

is contained in $P \cap \tilde{B}_2(x, \delta)$, and the reflected cone

$$C^-(h) := \{(x_1, x_2) : -h < x_2 < 0, |x_1| < -x_2/K_0\}$$

is contained in $(\mathbb{R}^2 \setminus P) \cap \tilde{B}_2(x, \delta)$. Moreover $|C^+(h)| = |C^-(h)| = h^2/K_0$.

If $\chi_Q \equiv 0$ on $\tilde{B}_2(x, \delta)$ then $C^+(h) \subset P \setminus Q \subset P\Delta Q$; if $\chi_Q \equiv 1$ on $\tilde{B}_2(x, \delta)$ then $C^-(h) \subset Q \setminus P \subset P\Delta Q$. In both cases, $|P\Delta Q| \geq h^2/K_0$ for $h = \min\{r_0, \delta/2\}$, which implies $\delta \leq 2\sqrt{K_0}|P\Delta Q|^{1/2}$ whenever $\delta \leq 2r_0$. If $\delta > 2r_0$, the same estimate with $h = r_0$ gives $|P\Delta Q| \geq r_0^2/K_0$ and thus $\delta \leq \text{diam}(\Omega) \leq \text{diam}(\Omega)\sqrt{K_0}/r_0 \cdot |P\Delta Q|^{1/2}$. Choosing $C_H = (\kappa - 1)^{-1/2} \max\{2\sqrt{K_0}, \text{diam}(\Omega)\sqrt{K_0}/r_0\}$ yields this lemma. \square

Lemma C.2. *There exist $C_{\text{vs}} > 0$ depending only on the a priori data in Remark 4.2 such that, if $P^0, P^1 \in \mathcal{A}_{1/2}$ with corresponding vertex list v^0 and v^1 , then their vertices can be ordered in such a way that*

$$\|v^0 - v^1\|_{\text{poly}} \leq C_{\text{vs}} d_H(\partial P^0, \partial P^1).$$

Proof of Lemma C.2. Let $\tilde{\mathcal{A}}_{1/2}$ be the non-strict relaxed class with parameters $(d_0/2, d_1/2, \beta_0/2)$, i.e., $\tilde{\mathcal{A}}_{1/2} = \{P \subset \Omega, \text{dist}(P, \partial\Omega) \geq d_0/2, |v_{i+1} - v_i| \geq d_1/2, \frac{\beta_0}{2} \leq \beta_i(v) \leq \pi - \frac{\beta_0}{2}, \partial P \text{ is simple}\}$. Therefore $\mathcal{A}_{1/2} \subset \tilde{\mathcal{A}}_{1/2}$. By Proposition 3.3 in Beretta and Francini [2022], there exist constants $\delta_0 > 0$ and $C_0 > 0$, depending only on the a priori data such that, if $P^0, P^1 \in \tilde{\mathcal{A}}_{1/2}$ satisfy $d_H(\partial P^0, \partial P^1) \leq \delta_0$, then the vertices can be ordered in such a way that

$$\|v^0 - v^1\|_{\text{poly}} \leq C_0 d_H(\partial P^0, \partial P^1).$$

It suffices to prove the case when $d_H(\partial P^0, \partial P^1) > \delta_0$. Suppose $d_H(\partial P^0, \partial P^1) > \delta_0$,

$$\|v^0 - v^1\|_{\text{poly}} \leq \|v^0\|_{\text{poly}} + \|v^1\|_{\text{poly}} \leq 2\text{diam}(\Omega) \frac{d_H(\partial P^0, \partial P^1)}{\delta_0}.$$

Taking $C_{\text{vs}} = \max(C_0, \frac{2\text{diam}(\Omega)}{\delta_0})$ finishes the proof. \square

Lemma C.3 (L^1 -stability under vertex perturbations). *Fix $P^* \in \mathcal{A}_{1/2}$ and consider the neighborhood $\varphi_{P^*}(U_{P^*})$ from Lemma 4.3. Let $v, w \in \varphi_{P^*}(U_{P^*})$ and set $\delta := \|v - w\|_{\text{poly}}$. Then*

$$\|\chi_{P(v)} - \chi_{P(w)}\|_{L^1(\Omega)} = |P(v)\Delta P(w)| \leq C\delta.$$

Here $C = 2n_v(\pi + 1)\text{diam}(\Omega) > 0$ is a constant.

Proof of Lemma C.3. Consider the segment $v(t) = (1-t)v + tw$ for $t \in [0, 1]$ and write $P_t := P(v(t))$. By Lemma 4.3, all $v(t)$ are relaxed admissible, thus P_t is well-defined and $P_t \subset \Omega$. Let $x \in P(v)\Delta P(w)$, we first show there exists $t^* \in [0, 1]$ such that $x \in \partial P_{t^*}$. Define

$$g(t) := \text{dist}(x, P_t^c) - \text{dist}(x, P_t),$$

where the map $t \mapsto g(t)$ is continuous. If $g(0) = 0$ or $g(1) = 0$, $x \in \partial P(v)$ or $x \in \partial P(w)$; otherwise $g(0)$ and $g(1)$ have opposite signs because x belongs to exactly one of P_0 and P_1 . Hence there exists $t^* \in (0, 1)$ such that $g(t^*) = 0$, which implies $\text{dist}(x, P_{t^*}) = \text{dist}(x, P_{t^*}^c) = 0$ and therefore $x \in \partial P_{t^*}$.

By Lemma B.1 we have

$$d_H(\partial P_{t^*}, \partial P(v)) \leq \|v(t^*) - v\|_{\text{poly}} \leq \delta,$$

so $\text{dist}(x, \partial P(v)) \leq \delta$. This shows

$$P(v)\Delta P(w) \subset \{x \in \mathbb{R}^2 : \text{dist}(x, \partial P(v)) \leq \delta\}.$$

Now $\partial P(v)$ is a union of n_v line segments. The δ -neighborhood of a segment of length ℓ has area at most $2\delta\ell + \pi\delta^2$ (rectangle plus two half-disks). Summing over all edges yields

$$|P(v)\Delta P(w)| \leq 2\delta \text{Per}(P(v)) + n_v\pi\delta^2.$$

Finally, $\text{Per}(P(v)) \leq n_v\text{diam}(\Omega)$ and $\delta \leq 2R_{P^*} \leq 2\text{diam}(\Omega)$ on the chart, hence $|P(v)\Delta P(w)| \leq C\delta$ with $C = 2n_v(\pi + 1)\text{diam}(\Omega)$. \square

We are now ready to prove Lemma 4.3.

Proof of Lemma 4.3. If $\|v - v^*\|_{\text{poly}} < R_{P^*}$, then $R_{P^*} \leq \rho_{P^*}$ implies $P(v) \in \mathcal{A}_{1/2}$ by Lemma 4.2, hence $\gamma_{P(v)} \in M$ and $U_{P^*} \subset M$.

Moreover, $R_{P^*} \leq \frac{1}{4} \min_{i \neq j} |v_i^* - v_j^*|$ implies that the balls $B_2(v_i^*, R_{P^*})$ are pairwise disjoint. Therefore each perturbed vertex v_i lies in exactly one ball of v_i^* , so no cyclic shift or reversal of the vertex labeling is possible inside U_{P^*} ; thus φ_{P^*} is well-defined injective. Next we show that φ_{P^*} is a homeomorphism.

(continuity of $\varphi_{P^*}^{-1}$). By Lemma C.3, the map

$$\varphi_{P^*}^{-1} : \mathcal{O}_{P^*} \rightarrow L^1(\Omega), \quad v \mapsto \gamma_{P(v)},$$

is (locally) Lipschitz in $L^1(\Omega)$ on \mathcal{O}_{P^*} , hence continuous.

(continuity of φ_{P^*}). For each γ_{P_0} in U_{P^*} , for any sequence γ_{P_k} in U_{P^*} converges to γ_{P_0} , $|P_k \Delta P_0| = \frac{1}{(\kappa-1)} \|\gamma_{P_k} - \gamma_{P_0}\|_{L^1(\Omega)} \rightarrow 0$. By Lemma C.1, $d_H(\partial P_k, \partial P_0) \rightarrow 0$, and then by Lemma C.2, we have $\|v^k - v^0\|_{\text{poly}} \rightarrow 0$ for some v^k and v^0 such that $P(v^k) = P_k$ and $P(v^0) = P_0$. Thus φ_{P^*} is continuous.

(U_{P^*} is open in M). For each γ_{P_0} in U_{P^*} , we show that γ_{P_0} is the interior point in U_{P^*} . Assume by contradiction that for every $k \geq 1$, there exists $\gamma_{P_k} \in M \cap B_{L^1}(\gamma_{P_0}, \frac{1}{k})$ such that $\gamma_{P_k} \notin U_{P^*}$. Then $\|v^k - v^*\|_{\text{poly}} \geq R_{P^*}$ for some v^k such that $P(v^k) = P_k$. By the triangle inequality we have

$$0 < R_{P^*} - \|v^0 - v^*\|_{\text{poly}} \leq \|v^k - v^0\|_{\text{poly}}, \quad k \geq 1, \quad (24)$$

for some v^0 such that $P(v^0) = P_0$. Since $\|\gamma_{P_k} - \gamma_{P_0}\|_{L^1(\Omega)} \rightarrow 0$, we have $\|v^k - v^0\|_{\text{poly}} \rightarrow 0$, which contradicts to Equation 24. \square

D Proof for Lemma 4.4

The following proof follows the idea in the Proof of theorem 3.1 from Alberti et al. [2022].

Proof. Let $(\gamma_{P_j})_j \subset K$ with $P_j = P(v^j)$ and $v^j = (v_1^j, \dots, v_{n_v}^j)$ the counterclockwise vertex list. Set $\Omega_{d_0} := \{x \in \mathbb{R}^2 : \text{dist}(x, \partial\Omega) \geq d_0\} = \overline{B(0, 1 - d_0)}$. By (A1) we have $P_j \subset \Omega_{d_0}$, hence $v_i^j \in \Omega_{d_0}$ for all i, j .

Since Ω_{d_0} is compact and there are only finitely many cyclic relabelings, we may pass to a subsequence indexed by j_m and relabel the vertices by a fixed cyclic shift so that $v^{j_m} \rightarrow v^*$ in \mathbb{R}^{2n_v} . Define $P^* := P(v^*)$ and we show that $P^* \in \mathcal{A}$.

- (A1) Since Ω_{d_0} is convex, $P^* = \text{conv}\{v_i^*\} \subset \Omega_{d_0} \subset \Omega$, and therefore $\text{dist}(P^*, \partial\Omega) \geq d_0$.
- (A2) For each i , the map $v \mapsto |v_{i+1} - v_i|$ is continuous, hence $|v_{i+1}^* - v_i^*| = \lim_j |v_{i+1}^j - v_i^j| \geq d_1$.
- (A3) For each i , the interior angle $\beta_i(v)$ is a continuous function of the adjacent edge vectors (as long as $|v_i - v_{i-1}|, |v_{i+1} - v_i| > 0$, ensured by (A2)). Thus $\beta_i(v^*) = \lim_j \beta_i(v^j)$ and $\beta_0 \leq \beta_i(v^*) \leq \pi - \beta_0$. Moreover, the uniform bound $\beta_i(v^*) \leq \pi - \beta_0$ rules out collinearity of adjacent edges, so P^* is a convex polygon with the same counterclockwise ordering, hence simple.

Thus $P^* \in \mathcal{A}$ and $\gamma_{P^*} \in K$.

Finally, by Lemma C.3, for large j_m we have $|P_{j_m} \Delta P^*| \rightarrow 0$, hence

$$\|\gamma_{P_{j_m}} - \gamma_{P^*}\|_{L^1(\Omega)} = |\kappa - 1| |P_j \Delta P^*| \rightarrow 0.$$

Therefore every sequence in K admits an $L^1(\Omega)$ -convergent subsequence with limit in K , so K is compact in $L^1(\Omega)$. \square

E Proof for Lemma 4.5

Proof of Lemma 4.5. Since $M \subset L^1(\Omega)$ is endowed with the L^1 -subspace topology (equivalently, the inclusion $\iota : M \hookrightarrow L^1(\Omega)$ is a continuous embedding), compactness of K in $L^1(\Omega)$ implies that K is compact in M .

For each $\gamma_P \in K$, the set

$$V_P = \left\{ \gamma \in U_P : \|\varphi_P(\gamma) - v^P\|_{\text{poly}} < \frac{1}{2}R_P \right\} = \varphi_P^{-1}(\{v : \|v - v^P\|_{\text{poly}} < \frac{1}{2}R_P\})$$

is open in M (it is the preimage of an open ball under the continuous chart map φ_P). Moreover $\gamma_P \in V_P$, hence $\{V_P\}_{\gamma_P \in K}$ is an open cover of K . By compactness of K in M , there exist $P_1, \dots, P_m \in \mathcal{A}$ such that $K \subset \bigcup_{i=1}^m V_{P_i}$.

Fix $i \in \{1, \dots, m\}$ and by the choice of R_{P_i} we have $B_i \subset \varphi_{P_i}(U_{P_i})$. Since B_i is compact in \mathbb{R}^{2n_v} and $\varphi_{P_i}^{-1}$ is continuous on $\varphi_{P_i}(U_{P_i})$, the set $\varphi_{P_i}^{-1}(B_i)$ is compact (hence closed) in M and contains V_{P_i} . Therefore

$$\overline{V}_{P_i} \subset \varphi_{P_i}^{-1}(B_i) \subset U_{P_i},$$

so φ_{P_i} is well-defined on \overline{V}_{P_i} .

Now $K \cap \overline{V}_{P_i}$ is closed in the compact set K , hence compact in M . By continuity of φ_{P_i} on U_{P_i} , the image

$$E_i = \varphi_{P_i}(K \cap \overline{V}_{P_i})$$

is compact in \mathbb{R}^{2n_v} . Moreover, from $\overline{V}_{P_i} \subset \varphi_{P_i}^{-1}(B_i)$ we obtain $E_i \subset B_i$, so $\bigcup_{i=1}^m E_i$ is bounded.

Finally, B_i is convex (a closed ball of a norm), hence $\text{conv}(E_i) \subset B_i$. Together with $B_i \subset \varphi_{P_i}(U_{P_i})$, this yields

$$\text{conv}(E_i) \subset \varphi_{P_i}(U_{P_i}), \quad i = 1, \dots, m.$$

□

F Proof for Lemma 4.10

Proof. Since $E \subset B_2(0, R)$, monotonicity of covering numbers gives $\mathcal{N}_\delta(E; \|\cdot\|_2) \leq \mathcal{N}_\delta(B_2(0, R); \|\cdot\|_2)$.

If $\delta \geq R$, then $B_2(0, R) \subset B_2(0, \delta)$, hence $\mathcal{N}_\delta(B_2(0, R); \|\cdot\|_2) = 1$.

Assume now $0 < \delta < R$. Let $\{x_j\}_{j=1}^n \subset B_2(0, R)$ be a maximal δ -separated set (i.e., $\|x_i - x_j\|_2 > \delta$ for $i \neq j$ and it is maximal by inclusion). By maximality, $\{x_j\}$ is a δ -net of $B_2(0, R)$, hence $\mathcal{N}_\delta(B_2(0, R); \|\cdot\|_2) \leq n$. Moreover, the balls $\{B_2(x_j, \delta/2)\}_{j=1}^n$ are disjoint and satisfy $B_2(x_j, \delta/2) \subset B_2(0, R + \delta/2)$, so a volume comparison yields

$$n \text{vol}(B_2(0, \delta/2)) \leq \text{vol}(B_2(0, R + \delta/2)) = \left(\frac{R + \delta/2}{\delta/2}\right)^{2n_v} \text{vol}(B_2(0, \delta/2)).$$

Therefore $n \leq (1 + 2R/\delta)^{2n_v}$. Since $\delta < R$ implies $1 + 2R/\delta \leq 3R/\delta$, we obtain $\mathcal{N}_\delta(B_2(0, R); \|\cdot\|_2) \leq (3R/\delta)^{2n_v}$. Combining the cases $\delta \geq R$ and $0 < \delta < R$ proves the claim for some absolute constant C_{vol} (e.g. one may take $C_{\text{vol}} = 3$). □

G Effect of the $1/\sqrt{N}$

Although the TV bound Equation 20 does not display an explicit dependence on the discretization level N (or the ambient dimension d_N), this is facilitated by the $1/\sqrt{N}$ normalization built into the measurement map F_N .

To illustrate its role, consider the unnormalized measurements

$$\tilde{F}_N(\gamma) := \sqrt{N} F_N(\gamma), \quad \tilde{F}_N(K) := \sqrt{N} F_N(K).$$

For every $\varepsilon > 0$, scaling implies

$$\mathcal{N}_\varepsilon(\tilde{F}_N(K); \|\cdot\|_2) = \mathcal{N}_{\varepsilon/\sqrt{N}}(F_N(K); \|\cdot\|_2).$$

Using the covering number bound from the proof of Theorem 4.12, there exists a constant $C > 0$ (independent of N) such that

$$\mathcal{N}_\eta(F_N(K)) \leq m \max \left\{ 1, \left(\frac{C}{\eta}\right)^{2n_v} \right\}.$$

Taking $\varepsilon = \epsilon_0 = T^{-c_{\epsilon_0}}$ yields an additional additive $n_v \log N$ term in $\log \mathcal{N}_{\epsilon_0}(\tilde{F}_N(K))$ (corresponding to the factor $(\sqrt{N})^{2n_v} = N^{n_v}$), while the intrinsic exponent $2n_v$ is unchanged. Similarly, the support radius rescales as $\sup_{\gamma \in K} \|\tilde{F}_N(\gamma)\|_2 = \sqrt{N} \sup_{\gamma \in K} \|F_N(\gamma)\|_2 \leq \sqrt{N} r_K$.